PCCP

PAPER

View Article Online
View Journal | View Issue

Cite this: *Phys. Chem. Chem. Phys.*, 2017, **19**, 12683

Doping of RE ions in the 2D ZnO layered system to achieve low-dimensional upconverted persistent luminescence based on asymmetric doping in ZnO systems

Bolong Huang

Open Access Article. Published on 19 April 2017. Downloaded on 9/18/2024 11:04:37 AM. This article is licensed under a Creative Commons Attribution-NonCommercial 3.0 Unported Licence.

Received 14th March 2017, Accepted 15th April 2017

DOI: 10.1039/c7cp01623a

rsc.li/pccp

Herein, we dope a low-dimensional ZnO system with a wide range of rare earth (RE) ions. Through systematic calculations, the dopable range of all ZnO systems was found to be asymmetrical, which accounts for the difficulty in achieving p-type doping. Low-dimensional ZnO systems, similar to 2D graphene-like nanosheets, have a wider doping limit. Thus, 2D ZnO is a promising candidate to achieve a wider doping range in ZnO. To further examine energy transfer in upconversion luminescence, the excited states of all lanthanide (Ln) elements in both the Ln^{2+} and Ln^{3+} ionic state in the bulk ZnO lattice were extensively studied. The probability of mixed valences of the Ln dopant ions occurring in ZnO was discussed, along with the analysis of the relative oscillator strengths. At the Ln^{2+} states, the heavy lanthanide elements usually dominated the energy transmission channel at high energy, the medium lanthanide elements mostly occupied the middle range of the optical fundamental gap, and the light lanthanide elements were widely spread over the optical band gap as well as the conduction band range. However, Ln^{3+} ions, as the sensitizing dopant, have reduced energy barriers for excited state absorption, showing wider energy transfer channels that are evenly distributed within 3.0 eV, which is lower than the conduction band edge absorption in Ln^{2+}. Meanwhile, each energy level has an obviously stronger oscillator strength, indicating a larger probability for excitation and energy transport between the inter-levels. Thus, in physicochemical and biological terms, trivalent Ln doping follows the removal of apical dominance concept, contributing more flexible energy transfer within the biological window for *in vivo* imaging or other related optoelectronic devices.

Introduction

ZnO, a transparent semiconducting oxide, has a wide band gap of 3.4 eV with a large exciton binding energy of 60 meV[1] and exhibits strong size-dependent electronic and optical properties. Currently, scientific interest in the flexibility and the size- and shape-controlled fabrication of nanomaterials is growing. Low-dimensional ZnO nanostructures have great potential for human-friendly nanodevices, biomedical science, and light-emitting devices that require extremely low power consumption.[2–4] Multi-scaled, low-dimensional ZnO, which can be produced using various novel fabrication technologies, has promising applications in solid-state, short-wavelength, light-emitting, transparent, conducting, and piezoelectric materials, as well as in room-temperature ultraviolet (UV) laser emission devices and UV photovoltaic cells with tailored dimensions.[5–9] Due to its biocompatibility and luminescence, which is often applied in biomedical science, ZnO has potential in biophotonics and biomedical applications for imaging living cells and tissue.[10]

Recent experiments have shown that ZnO exhibits both two-photon absorption (TPA) and two-step two-photon absorption (TS-TPA) photon upconversions (UCs) with a tunable and energy-efficient UC mechanism that persist even at low excitation density.[11,12] These pioneering experiments shed light on opportunities for modulating and improving the output luminescence and device applications of ZnO nanomaterials.

UC has rapidly attracted great research interest in a number of fields, with a focus on applications such as bioprobes, drug delivery, tumor positioning in anti-cancer research, and opto-electronics.[11–24] Ln^{3+}-doped or Ln^{3+}-based UC nanoparticles (UCNPs) are of great interest for bioprobes, as they respond to a wide range of stimuli[13–18] and are superior to conventional quantum dots and organic dyes, whose luminescence is sensitive to their size and chemical surroundings.[4,19–21] Due to their near infrared (NIR) emission and deep penetration depths by long wavelengths, UCNPs offer minimized photodamage, high signal-to-noise

Department of Applied Biology and Chemical Technology, The Hong Kong Polytechnic University, Hong Hum, Kowloon, Hong Kong SAR, China. E-mail: bhuang@polyu.edu.hk

Open Access Article. Published on 19 April 2017. Downloaded on 9/18/2024 11:04:37 AM.

This article is licensed under a Creative Commons Attribution-NonCommercial 3.0 Unported Licence.

ratios and remarkable penetration depths for *in vitro* and *in vivo* applications,[22–27] bioprobes,[19,28] and drug delivery[29,30] in biological chemistry and in biomedical treatment/therapy in anticancer research.[19,22,26,31–36] The biosafety of UCNPs is relatively stable, as determined by biotests,[26,37] and UCNPs present low nanotoxicity, as noted in a recent review.[38] In addition, UCNPs also exhibit promising applications in solar cells due to their enhanced energy conversion efficiency resulting from their ability to absorb solar light in the infrared region.[39] Combinatorial approaches have recently been developed to quickly screen UCNP candidates for biological applications *via* high-throughput screening, modeling and applications using tailored 96-well microplate parallel synthesis systems.[40]

In fact, native energy transfer events in Ln^{3+}-doped UCNPs dominate the UC efficiency,[21] and the high-throughput synthesis and screening of applicable UCNP candidates leads developments to remain in the experimental trial phase, as different energy transfer pathways may vary the output color of UC emissions because emission can proceed *via* various photoelectron transport mechanisms.[41] However, energy transfer studies can manipulate the UC through guided theoretical energy transfer mechanisms to achieve satisfactory efficiency and the desired output color.

Epitaxial techniques are considered promising methods for producing ZnO thin films for optoelectronic devices. In comparison with conventional vapor-phase deposition methods, solution-deposition techniques, such as chemical bath deposition (CBD), have attracted attention because of their low-cost setup, low processing temperature, high productivity, and scale-up potential, especially for ZnO thin films grown on glass substrates.[25] Moreover, if the substrate is pre-seeded with ZnO crystallites or a small amount of transition metal ions, such as Fe^{2+} or Fe^{3+}, drawbacks of CBD, such as the irreproducible heterogeneous growth of the ZnO film, can be overcome.[26–28]

The microemulsion-mediated hydrothermal approach is another convenient route. A number of remarkable studies have reported that $Zn(OH)_4{}^{2-}$ and $Zn(NH_3)_4{}^{2+}$ can be used as precursors in solution and have detailed simple strategies to obtain tunable, multi-scaled, low-dimensional ZnO nanomaterials.[29–35] Zero-dimensional (0D) nanoparticles as well as two-dimensional (2D) nanoplates or nanosheets can be obtained *via* the oriented attachment mechanism under hydrothermal conditions by the following synthetic pathway:[29–35]

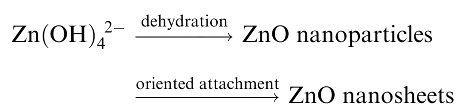

$$Zn(OH)_4{}^{2-} \xrightarrow{\text{dehydration}} \text{ZnO nanoparticles} \xrightarrow{\text{oriented attachment}} \text{ZnO nanosheets}$$

Following the above route, well-crystallized and monodisperse nanoparticles can be obtained through Ostwald ripening. This synthetic strategy exhibits certain flexibility in controlling the morphology and can tune the dimension of ZnO to either one-dimensional (1D) or 2D nanocrystals. Hao *et al.* also attempted a similar route, obtaining a different morphology.[35]

Here, we emphasize that intermediates in the synthesis of layered structural materials can act as generalized precursors, and outline a universal synthetic method to obtain 2D ultrathin nanomaterials, which can be applied to obtain ZnO with a 2D layered structure.[36] The findings recently reported by Yan *et al.*[36] not only allow the fabrication of a controllable ultrathin 2D nanomaterial but also contribute a cornerstone material for related fundamental studies on the properties and performances of these materials, as well as the future exploration of new materials through this facile synthetic route.

To date, the energy levels of lanthanide (Ln) dopants in ZnO-related nanomaterials, including the thermodynamic transition levels, single-particle levels, and excitation levels, have not been thoroughly studied. In particular, the nature and mechanism of emission induced by different energy transfer events *via* Ln^{2+} in the ZnO system has not been well interpreted through theoretical studies. Therefore, it is necessary to explore and understand the intrinsic dopable range of lanthanide ions and the excitations that lead to specific UC energy transfer properties.

The n-type doping of ZnO can be achieved through electronic modulation, while p-type doping is very difficult to achieve.[37,38] One of our collaborators suggested that this difficulty may be due to asymmetric doping behavior resulting from native point defects, especially oxygen vacancies (V_O) and zinc vacancies (V_{Zn}).[39,40] Synthesized ZnO usually presents intrinsic n-type semiconducting behavior,[41,42] which may be due to intrinsic defects or hydrogen (H) atoms produced during synthesis.[43,44]

Bulk ZnO materials typically have two common crystal phases: zincblende or wurtzite. Both phases show direct band structures at the Γ point of the Brillouin zone (BZ).[45] However, the optoelectronic applications of these materials are affected by their limitations in p-type doping. These limitations arise from native point defects, which control the boundary of the bi-polar doping limit (n-/p-doping limit) and are largely composed of intrinsic lattice defects, such as vacancies or interstitials.[37] The Fermi level cannot be easily modified by extrinsic dopants due to the spontaneous formation of numerous native point defects, which influences the n-/p-doping limit.[39]

Other lattice systems can be fabricated, such as the rock-salt lattice, which can be obtained under high pressures of approximately 9–10 GPa, and the 2D graphene-like ZnO lattice, which can be obtained using molecular beam epitaxial growth or the microemulsion hydrothermal method. Moreover, amorphous semiconductor thin films, such as amorphous ZnO (am-ZnO), have relaxed k-selection rules and optical transition constraints, endowing these materials with unique advantages over crystalline thin films or bulk materials. Additionally, the sample preparation of am-ZnO has a lower cost and can be amended to produce large-area sheets or thin films.[46] Furthermore, solid am-ZnO shows a better light conversion efficiency and improved energy transitions between inter-level excitations. Herein, we perform a preliminary study on the intrinsic dopable range in am-ZnO.

To study the persistent luminescence of ZnO, the defect process and dynamics under external photoirradiation must be understood. Charge transfer and energy transport must be interpreted *via* accurate calculations of the energy levels with

Open Access Article. Published on 19 April 2017. Downloaded on 9/18/2024 11:04:37 AM.
This article is licensed under a Creative Commons Attribution-NonCommercial 3.0 Unported Licence.

and without doping (*e.g.*, n- or p-type doping).[47,48] On the other hand, these calculations require a systematic study of a range of native point defect levels in terms of the single-particle levels (SPL), thermodynamic transition levels (TTL), and optical vertical excitation levels under the Franck–Condon framework.[48] Moreover, to estimate the energy formation cost, note that native point defects depend on the specific chemical potential limit and the local structural relaxation and cross-section of defects that capture charge carriers. Our recently developed model shows that the long-decay recombination behavior of excited electron–hole pairs occurs through a time-accumulated donor–acceptor band, which has been continuously pumped by local lattice distortions with a corresponding negative effective correlation energy.[49–51] Our model not only combines a lattice relaxation model resulting from defects such as DX and EL2 centers[52,53] and an energy barrier model involving the photo-generated Coulomb potential from electron–hole pairs,[54–56] but also shows a potential zero-phonon line electronic inter-band transition, which can explain the energy conversion mechanism leading to persistent luminescence.

To achieve a better combination of experimental observations and theoretical studies, electronic structure calculations are necessary for each given ZnO system. As is well known, the electronic structure of a given semiconductor material plays a significant role in determining its potential applications. Correct band structures and defect levels are important for experimentalists engaging in defect engineering to tune the electronic properties through extrinsic doping. However, the doping limits determined by the native point defect levels are still unknown. Therefore, we herein extend the doping limit study to several ZnO systems to determine how the doping limit varies with the symmetry and dimension of ZnO solid systems *via* density functional theory (DFT) calculations.

Calculation setup

Ground state structure optimization

Our defect-state structural relaxation and formation energy calculations were performed using the CASTEP code.[57] Norm-conserving pseudopotentials of Zn and O were generated by the OPIUM code in the Kleinman–Bylander projector form,[58] which employs a non-linear partial core correction on the fully closed $3d^{10}$ shell[59] and a scalar relativistic averaging scheme[60] to account for spin–orbital coupling effects. The Rappe–Rabe–Kaxiras–Joannopoulos (RRKJ) method was chosen to optimize the pseudopotentials.[61] The PBE functional was chosen for PBE+U calculations, with a kinetic cutoff energy of 750 eV, which expands the valence electron states in a plane-wave basis set. The ensemble DFT (EDFT) method of Marzari *et al.*[62] was used for convergence when considering the am-ZnO system. To obtain the bulk properties of WZ-ZnO, we used a $9 \times 9 \times 6$ Monkhorst–Pack (MP) k-point mesh, where the total energy convergence of each atom was under 5.0×10^{-7} eV. For the electronic structure calculations of the 2D layered ZnO system, we examined a $4 \times 4 \times 1$ supercell after the total energy convergence calculations using our developed pseudopotentials[63] with a 750 eV cutoff energy. The Hellmann–Feynman force on each atom was converged to lower than 0.01 eV Å^{-1}. To calculate the defects in am-ZnO, we used a simple cubic cell containing 64 atoms. We selected the $(\frac{1}{4}, \frac{1}{4}, \frac{1}{4})$ special k-point[64] in the simple cubic cell. Geometry optimizations used the Broyden–Fletcher–Goldfarb–Shanno (BFGS) algorithm through all bulk and defect supercell calculations.

Hubbard-*U ab initio* determination at each Zn and O site

As determined in the theoretical studies, the electronic and localized defect states that occur in the optical fundamental gap were less sensitive to the nonlinearity or orbital coupling of Hubbard U parameters. Thus, the rotational-invariant DFT+ Hubbard U (DFT+U) method was used, which follows the Anisimov-type approximation.[65] To remove side effects of the localized hole states produced by the 2p orbitals of O sites, the self-consistently determined Hubbard U potentials were also applied to the O-2p orbitals, which is a common practice[66–69] for many oxide materials. Therefore, self-energy corrections of both the d- and p-orbitals of the various forms of zinc oxides, especially the amorphous structures, must be considered.[63,70–72] We have carried out series of *ab-initio* calculations on the on-site orbital Coulomb potential parameter (*i.e.* Hubbard U) in any given structures. This process returns the self-consistent parameters on each Zn and O sites based on our previously developed method.[71,72]

Defect formation enthalpy formula

We used the equation developed by Zunger *et al.*[73] to calculate the defect formation energy at different charge states (q). The overall supercell was established and remained fixed for all lattice parameters based on the ground state relaxed primitive cell to reduce the effect of enthalpy changes resulting from cell variations. The formation energy of a target defect (H_q) at a specific charge state q can be described as the relation between the Fermi energy level (E_F) and the chemical potential $\Delta\mu$ of defect species α, which is described as follows:

$$H_q(E_\text{F},\mu) = \left[E_q - E_\text{H}\right] + q(E_\text{V} + \Delta E_\text{F}) + \sum_\alpha n_\alpha\left(\mu_\alpha^0 + \Delta\mu_\alpha\right). \quad (1)$$

The variables E_q and E_H are the total energy of a relaxed defective lattice with charge state q and the corresponding ideal lattice (defect-free) in the ground state, respectively; ΔE_F is the change in the Fermi energy with respect to the valence band maximum (VBM, $E_\text{V} = 0$) with the formation of the defect; n_α is the number of atoms of element α chosen as target defect sites; and finally, μ_α^0 is the reference chemical potential of the element α.

Charge point defect corrections within the periodic lattice

In the case of defects with $q \neq 0$, a Coulomb potential correction is required to counteract the effects from the image charge of the crystal lattice. To date, three corrections have been developed. One is the band alignment correction developed by Van de Walle and coworkers.[74] The second is the dispersion correction of

defects between the gamma point and Monkhorst–Pack point, developed by Wei *et al.*[75] The third is the dipole correction, which considers the Madelung effect based on static electric Coulomb potential corrections, developed by Makov and Payne;[76] this method is the current popular correction scheme in DFT and is used by us in this work. However, such image charge corrections contribute only around ~0.2 eV in magnitude to the defect formation energy. Our goal is to establish a physicochemical trend, rather than highly accurate level calibrations, which require demanding computations.

Results and discussion

Ground state electronic properties

We first examined the electronic structures of ZnO in different lattice systems and compared the band structures of wurtzite (WZ), zincblende (ZB), rock-salt (RS) and 2D monolayer ZnO, as shown in Fig. 1. RS ZnO was shown to have an indirect minimum band gap from $L \rightarrow \Gamma$ of the BZ, where the conduction band minimum (CBM) is at the Γ point. This arises because the O sites have 6-fold octahedral coordination, which deviates from the common 4-fold tetrahedral coordination of WZ-ZnO, as shown in Fig. 1. The O-2p orbitals have largely re-distributed energy levels along the new BZ in RS ZnO, compared with WZ ZnO. Therefore, the VBM of RS-ZnO, which mainly consists of O-2p orbitals, is different from that of WZ ZnO and does not occur at the Γ point.

Fig. 2 shows the total electronic density of states (DOS) of ZnO in the different lattice systems. We further introduced an am-ZnO model for comparison. Both ZB and RS ZnO present van Hove singularities at the Zn-3d t_{2g} levels, showing $\nabla_k E = 0$ near the highly symmetrical $L \rightarrow \Gamma \rightarrow X$ points. In the amorphous system, the long-range order of the Zn and O sites is lost, while the local structures maintain short-range bonding angles and lengths similar to those of the ZnO single crystal. Thus, the Zn-3d t_{2g} levels of am-ZnO appear as broadened and less intense peaks, starting from 6.8 eV below the VBM.

As the electronic properties of WZ ZnO with native point defects have been studied in previous works,[40,77] we further examined the formation energies of native point defects in relation to the Fermi level (E_F) of WZ ZnO under different charge states

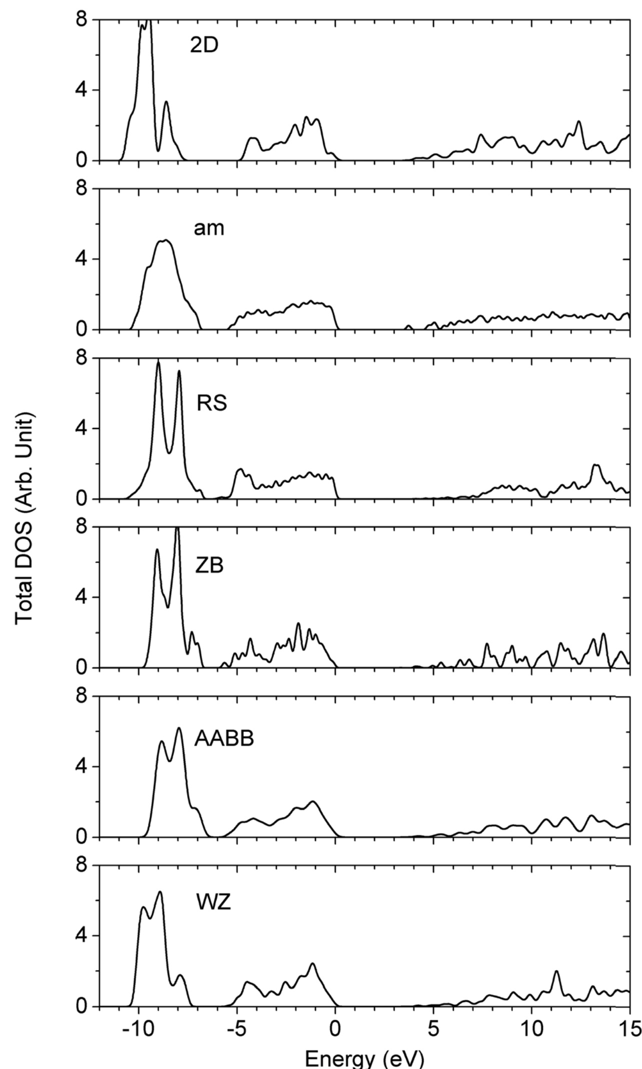

Fig. 2 The calculated total density of states (TDOSs) of wurtzite (WZ), AABB, zinc-blend (ZB), rock-salt (RS), amorphous (am) and two-dimensional monolayer (2-D) ZnO systems.

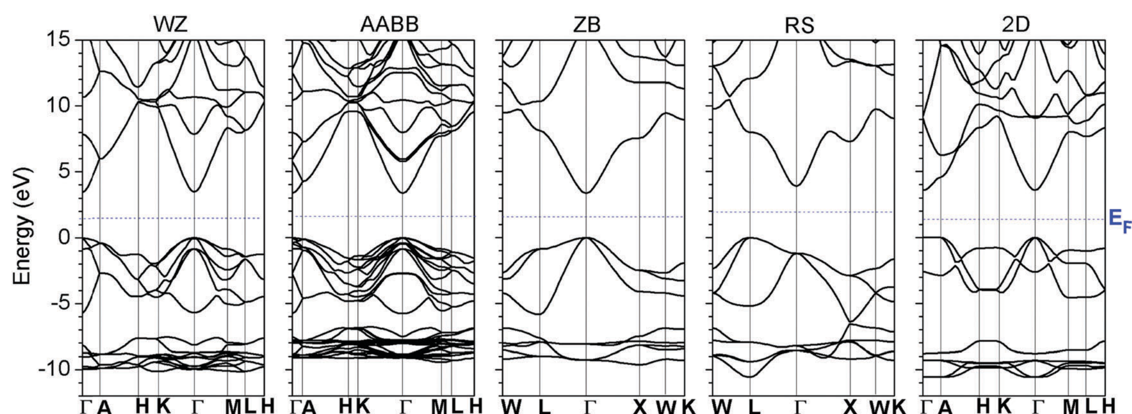

Fig. 1 The calculated band structures of wurtzite (WZ), AABB, rock-salt (RS), and two-dimensional monolayer (2-D) ZnO systems.

Open Access Article. Published on 19 April 2017. Downloaded on 9/18/2024 11:04:37 AM.
This article is licensed under a Creative Commons Attribution-NonCommercial 3.0 Unported Licence.

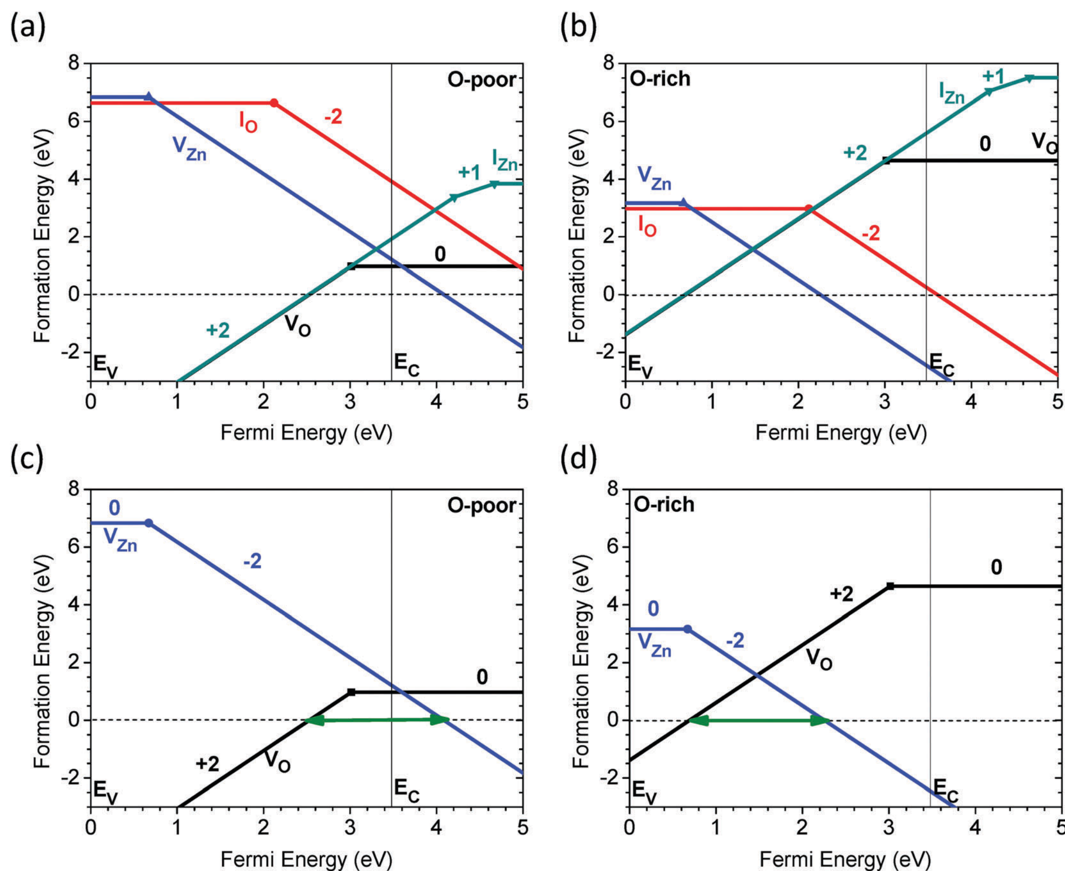

Fig. 3 Summary of native point defects in WZ-ZnO in O-poor (a) and O-rich (b) chemical potential limits. Summary of doping limits determined by native point defects in both O-poor (c) and rich (d) limits, denoted by green arrows.

Open Access Article. Published on 19 April 2017. Downloaded on 9/18/2024 11:04:37 AM. This article is licensed under a Creative Commons Attribution-NonCommercial 3.0 Unported Licence.

and chemical potential limits, which is typically done when considering the formation energies of native point defects. For comparison with other calculation methods using hybrid-functional DFT,[40,78] the formation enthalpy ΔH_f of WZ ZnO is −3.67 eV, which is much closer to the experimental data of −3.60 eV at 300 K. The direct band gap was found to be 3.44 eV from the band structure calculation based on the method we developed[71,79] using the new pseudopotential for Zn, as discussed in our previous report,[63] and the Zn-3d t_{2g} level started from 7.1 eV below the VBM (E_V −7.1 eV).

Native point defects and dopable range in WZ ZnO

As seen in Fig. 3(a), the formation energy of oxygen vacancies (V_O) is 0.98 eV in the neutral state under the O-poor limit, which gives a reasonable prediction of the defect concentration at approximately 900 K and is consistent with experimental data.[80,81] The defect with the second lowest formation energy is zinc interstitials (I_{Zn}), with a value of 3.84 eV, and the (+/0) transition level within the conduction band (CB) is located at E_V +4.21 eV, where E_V = 0 at the VBM. I_{Zn} is a possible donor source that provides charge carriers by donating electrons. However, in our calculations, the formation energy of I_{Zn} in the neutral state is relatively high and is nearly 2 eV higher than that of V_O. Meanwhile, V_O does not provide any mobile charges and instead contains strongly bound electrons that possess a negative U_{eff} (U_{eff} = −0.65 eV), showing a spin-paired correlation that cannot be detected by electron spin resonance (ESR) measurements.[82] Moreover, V_O^{2+} and I_{Zn}^{2+} have almost the same formation energy trends in relation to E_F, indicating their similar behavior as defect trap centers within the ZnO lattice. This finding implies that most experimental research has misunderstood the role of V_O and I_{Zn} as donor centers due to their similar behavior.[81,82] Fig. 3(b) shows that V_{Zn} and I_O are negatively charged defects with relatively low formation energies of 3.16 eV and 2.97 eV, respectively, under the O-rich limit. These defect sites also present negative U_{eff} features with −1.04 eV and −1.58 eV, respectively.

Next, we considered the doping limit in WZ ZnO, as shown in Fig. 3(c). When E_F is raised to the CBM by a donor dopant, the n-type doping limit (upper bound) is the point at which negatively charged native point defects spontaneously form to compensate for the charge. Thus, either V_{Zn} or I_O determines the n-type limit energy level. Considering the band gap area, V_{Zn} has a neutral formation energy similar to I_O. However, due to the shallower (0/2−) transition level at E_V +0.67 eV compared with that of I_O, V_{Zn}^{2-} shows enhanced stability within the band gap area. Therefore, $E_F = E_V$ +4.09 eV is the critical point at which V_{Zn}^{2-} spontaneously forms to compensate for the n-type dopant under the O-poor limit, while the critical point is $E_F = E_V$ +2.25 eV under the O-rich limit.

Similarly, for p-type dopants (acceptors), E_F is lowered to the VB edge E_V, and as E_F varies, donor defects, such as V_O and I_{Zn},

View Article Online

Open Access Article. Published on 19 April 2017. Downloaded on 9/18/2024 11:04:37 AM. This article is licensed under a Creative Commons Attribution-NonCommercial 3.0 Unported Licence.

will spontaneously form to compensate for the charge if relatively low formation energies are reached. Accordingly, in the O-poor limit, the lower bound of the doping limit is determined by V_O^{2+} due to its slightly lower formation energy in the band gap area compared with I_{Zn}^{2+}. Therefore, the p-type limit energy levels are 2.53 eV and 0.21 eV. Note that Robertson *et al.* showed that the lower bounds of the E_F area are 1.80 eV and 0.20 eV, respectively.[39] This difference arises in the O-poor limit because the formation energy of V_O, determined by the pure Zn-rich chemical limit, is relatively low in the neutral state at 0.85 eV, which is 0.1 eV lower than most of the reported DFT calculation results.[42,83] The source of error may be the formation enthalpy of −3.37 eV given previously,[39,40] which is 0.32 eV higher than that found experimentally. Compared with our calculated values of 4.09 eV and 2.25 eV for the n-type limit at different chemical potential limits, their source of error results from their formation energies of V_{Zn} at the various charge states being too high, which led to a wider range for the upper bound of the doping limit (n-type limit).[40] We have discussed doping limits in other systems, which were then used to achieve persistent luminescence *via* doping.[84]

The RS ZnO system does not have a doping limit at which to tune the Fermi level pinning boundary by extrinsic doping. Moreover, this system has an indirect band gap, which lowers the optical vertical transition efficiency *via* k-selection rules. Thus, this system was not considered.

Native point defects in amorphous ZnO

We then examined continuous random ZnO networks (CRN-ZnO) as more realistic am-ZnO models. For this work, we built short-range disordered ZnO in a 64-atom supercell using the RS ZnO lattice. The RS structure has many possible distortion directions, and there are many ways to generate distorted ZnO models. The building and generation of an amorphous model structure is an art in and of itself, as summarized by Drabold *et al.*, and usually requires equilibration over long time periods to achieve dynamic randomization and geometry relaxation at 0 K to guarantee that high-energy features of the structural configuration are mostly absent.[85] Am-ZnO structures have many potential applications. Thus, there are numerous generation paths for modeling the amorphous structures, which means there may be no universal method for generating amorphous metal oxide materials for a specific purpose. Falk *et al.* showed a recent example with a much more elaborate generation of am-ZnO structures.[86]

Ab initio molecular dynamics (MD) are typically used to model experimental environments. Here, am-ZnO was obtained using MD simulations with a 64-atom supercell ($Zn_{32}O_{32}$). First, the volume of the ideal 64-atom RS ZnO cell was held constant using the experimentally reported density, and the cell was melted at 1500 K for 2.5 ps (time interval of 1 fs). Second, the supercell was simulated at 600 K for 1 ps to represent an annealing process. Third, the model was further simulated at 300 K for 4 ps to obtain thermal equilibrium. The final structure was obtained after geometry relaxation by varying the cell size at the ground state. In the final structure, the weighted average coordination numbers of Zn and O were 3.6 and 3.5, respectively. Nearly 44% of the Zn sites were 4-fold coordinated with tetrahedral configuration, and nearly 50% of the O sites had tetrahedral configuration. The Zn and O coordination numbers of am-ZnO were lower than those of WZ-ZnO at around 3.

We next considered native point defects in am-ZnO, as well as their influence on the electronic properties. By projecting each orbital component of the electrons in the defective systems, we illustrated the partial density of states (PDOS) of am-ZnO with oxygen and zinc vacancies at different charge states.

As seen in Fig. 4(a) and (b), the difference in the coordination of the O vacancies leads to localized defect states with slightly different depths. The higher the V_O coordination number, the deeper the donor-like trap levels within the band gap. The 4-fold coordinated O vacancy (V_{O4}) has a trap level of E_V +2.17 eV, where E_V = 0 at the VBM, while V_{O3} has a defect trap level of E_V +2.29 eV. Moreover, the localized defect states are contributed by the components of the p- and s-orbitals of the two electrons on the adjacent 3 or 4 Zn sites. Compared to V_O^0 in the WZ ZnO system, the trap levels of V_{O4} and V_{O3} in am-ZnO are 0.1–0.2 eV deeper than the trap level in WZ ZnO (E_V +2.38 eV) according to our PDOS calculations. Moreover, the perturbed hole states (PHSs) are approximately 0.2 eV below the CBM, similar to the results of Lany and Zunger.[48]

Fig. 4(c) and (d) shows the two different charge states of V_{Zn} in am-ZnO. The neutral Zn vacancy (V_{Zn}^0) in am-ZnO indeed acts as an extra deep acceptor next to the CB edge (0.2 eV higher than the CBM), with contributions from the two different p-orbitals of the hole states localized on the adjacent O atoms. Similarly, V_{Zn}^0 in WZ ZnO is located at the CB edge. For V_{Zn}^- in the am-ZnO system, the localized hole state is reported to be localized on only one of the adjacent O sites or delocalized over the system, depending on the calculation level and modeling of the self-energy of the electrons in the orbitals.[63,71,79,84] V_{Zn}^{2-} in am-ZnO captured two electrons in the neutral state of the defect, acting as an acceptor-like trap.[80] In Fig. 4(d), the two captured electrons are localized right up to the VBM with energy intervals of approximately 0.1 eV due to contributions from the components of the p- and partially filled d-orbitals of the adjacent Zn and O sites.

Fig. 5 shows the charge density of the above defects in am-ZnO in different charge states. The relaxations of adjacent Zn ions next to V_O in am-ZnO are illustrated by arrows, indicating a strong Coulomb repulsive interaction of each nearby Zn ion when the localized electrons are ionized away (V_O^{2+} in am-ZnO). V_{Zn}^0 in ZnO induces two localized hole states in the p-orbitals of two adjacent O sites in different spin-up and spin-down configurations, respectively. The charge density of V_{Zn}^- confirms that the single localized hole is present in the p state at only one of the adjacent O sites, which is consistent with the results of Clark *et al.*[40] In the V_{Zn}^{2-} state of am-ZnO, two additional electrons fill not only the p-orbitals of the O sites but also the d-orbitals of the second nearest neighboring Zn sites; thus, the charge density of V_{Zn}^{2-} shows the co-existence of p- and d-orbitals of the localized states.

2D monolayer ZnO system

As is well known, ZnO is a wide-band-gap semiconductor oxide with a direct gap of approximately 3.4 eV (at 300 K), and

 This journal is © the Owner Societies 2017

Open Access Article. Published on 19 April 2017. Downloaded on 9/18/2024 11:04:37 AM.
This article is licensed under a Creative Commons Attribution-NonCommercial 3.0 Unported Licence.

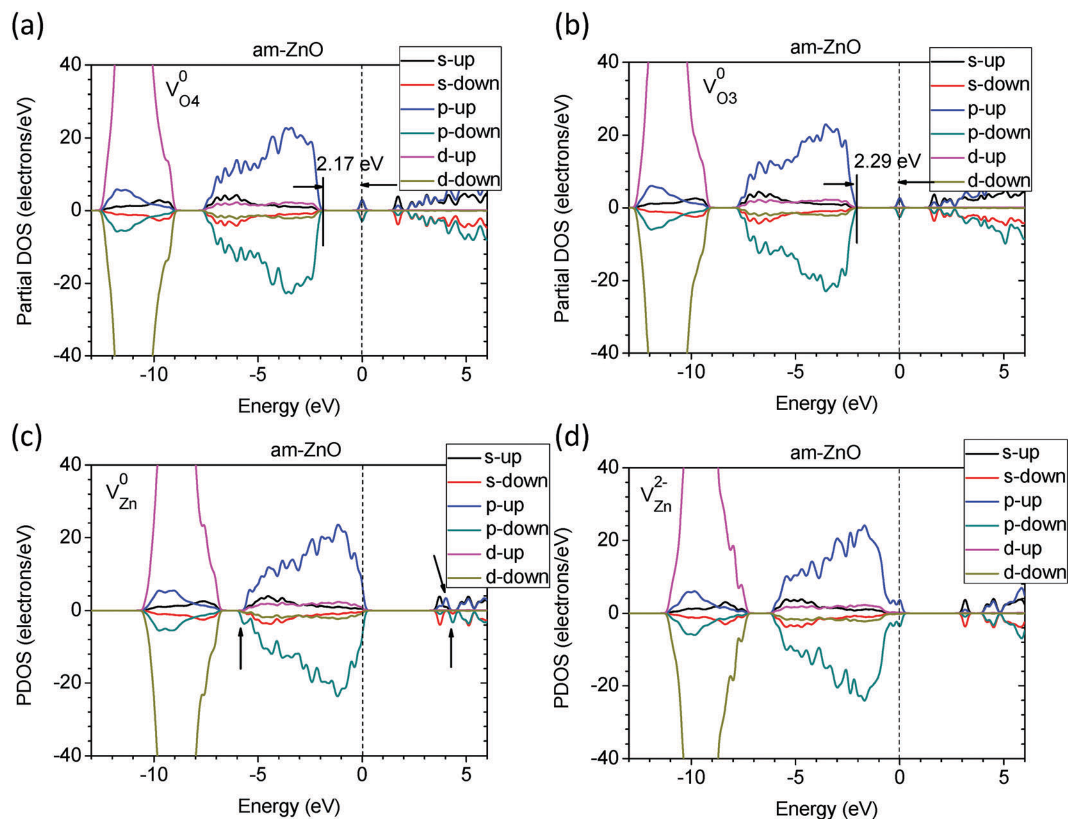

Fig. 4 The calculated partial DOSs (PDOSs) of am-ZnO with V_{O4} (a) and V_{O3} (b) in neutral states. The PDOSs of am-ZnO with V_{Zn} in neutral (c) and −2 charge (d) states.

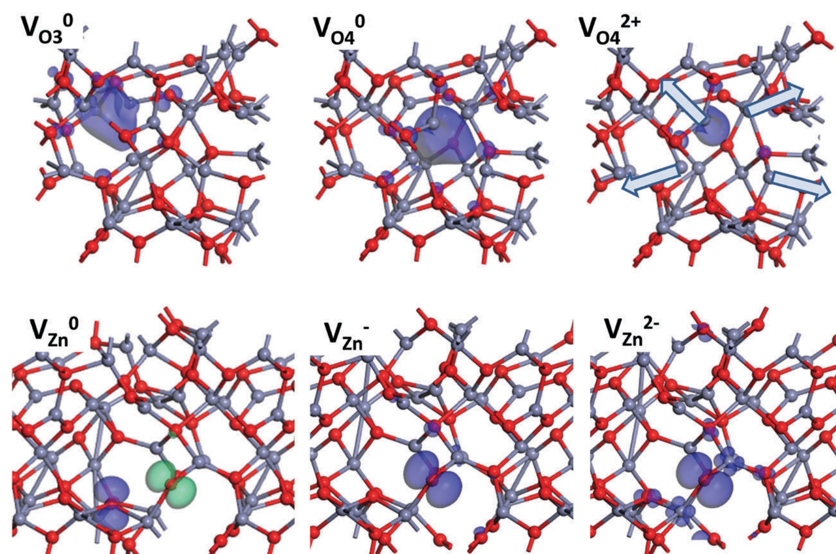

Fig. 5 Charge density of the 3-fold and 4-fold coordinated oxygen vacancy (V_{O3} and V_{O4}) for its neutral and 2+ charge states. The relaxation of Zn ions is indicated by arrows. Charge density of the Zn vacancy (V_{Zn}) for its neutral (with spin-up and spin-down), 1−, and 2− charge states. The charge density of V_{Zn}^- is a p-state localized on only one of the adjacent oxygen atoms (Zn = grey and O = red).

its monolayer can be used as a charge trapping layer in CMOS memory cells. Recently, many studies have shown that low-dimensional ZnO nanomaterials can be synthesized and present promising potential in renewable energy or electronics applications, for example, the near 0D quantum dot synthesized by Dutta *et al.*,[87] the 1D nanowire synthesized by Hwang *et al.*,[88] and the 2D nanolayer synthesized by Lau *et al.*[89] The physicochemical trends of the 2D ZnO system have shown that

Open Access Article. Published on 19 April 2017. Downloaded on 9/18/2024 11:04:37 AM. This article is licensed under a Creative Commons Attribution-NonCommercial 3.0 Unported Licence.

2D ZnO can be tuned to be both n- and p-type, presenting doping flexibility.[89] Moreover, the formation stability of the ideal 2D monolayer ZnO system has been studied and predicted by first-principles calculations.[90–93] Meanwhile, interfacial charge transfer between monolayer ZnO and graphene is a promising method for 2D electronic modulation with application in high-speed electronic response devices.

As shown in Fig. 6(a) and (b), the band structure and density of states show tail states due to the absence of long-range crystal field interactions vertically along ZnO(0001), and the 3d levels are split into two peaks due to an evident difference in p–d coupling along and perpendicular to ZnO(0001). The band gap increased to 3.57 eV, in comparison to the bulk phase value of 3.44 eV, which was determined from our calculations. The start of the 3d level is 0.5 eV deeper than that in the bulk (*i.e.*, −7.0 eV by calculation). The formation entropy of bulk ZnO is −3.70 eV, which is consistent with the experimentally reported value of −3.60 eV at 300 K. Fig. 1 and 2 give the basic electronic properties of bulk WZ and monolayer ZnO, respectively.

The oxygen hole levels in metal oxides and wide-band-gap semiconductors have long been of interest, particularly those in ZnO,[94,95] where the localized hole levels drive the Fermi level deeper in the gap. We investigated a single zinc vacancy (V_{Zn}), as this state can induce two holes localized at nearby O sites. However, this state cannot be clearly modeled by LDA/GGA calculations, as the homogeneous electron gas treats the two hole states as degenerate and delocalized around the V_{Zn} site. Our GGA+U calculation stabilizes the hole states and produces clear electron–hole interactions under different charge states, as shown in Fig. 6(a). This result has also been reported in our previous works.[63,70,71,79,84] Fig. 6(b) shows that neutral V_{Zn} has a negative effective correlation U (negative U_{eff}) value of −0.57 eV for the process of $2(V_{Zn}^0) \rightarrow (V_{Zn}^+) + (V_{Zn}^-)$. Such exothermal reaction indicates that one of the O sites, which are the nearest neighbors of V_{Zn}^0, acted as an acceptor, capturing two electrons and easily overcoming the onsite Coulomb repulsive energy. The other two localized hole states were repulsive, while the electron acceptor sites moved towards the hole sites. This behavior induces a planar Jahn–Teller distortion effect, where the symmetry is reduced from D_{3h} to D_{2h}. The other two charge states, V_{Zn}^+ and V_{Zn}^-, also show the same trend. The total energy of the system decreases during the structural relaxation. As seen in Fig. 6(c), the localized hole states have π-like orbitals near the CBM that are perpendicular to the (0001) plane in real space, showing p_z-orbital character (with a_1 symmetry). However, the electron acceptor site has a similar π-like orbital along the (0001) plane, which is a feature of the p_{xy}-orbital. This interesting behavior gives the monolayer ZnO system with the existence of a single neutral V_{Zn} antiferromagnetic (AFM) features.

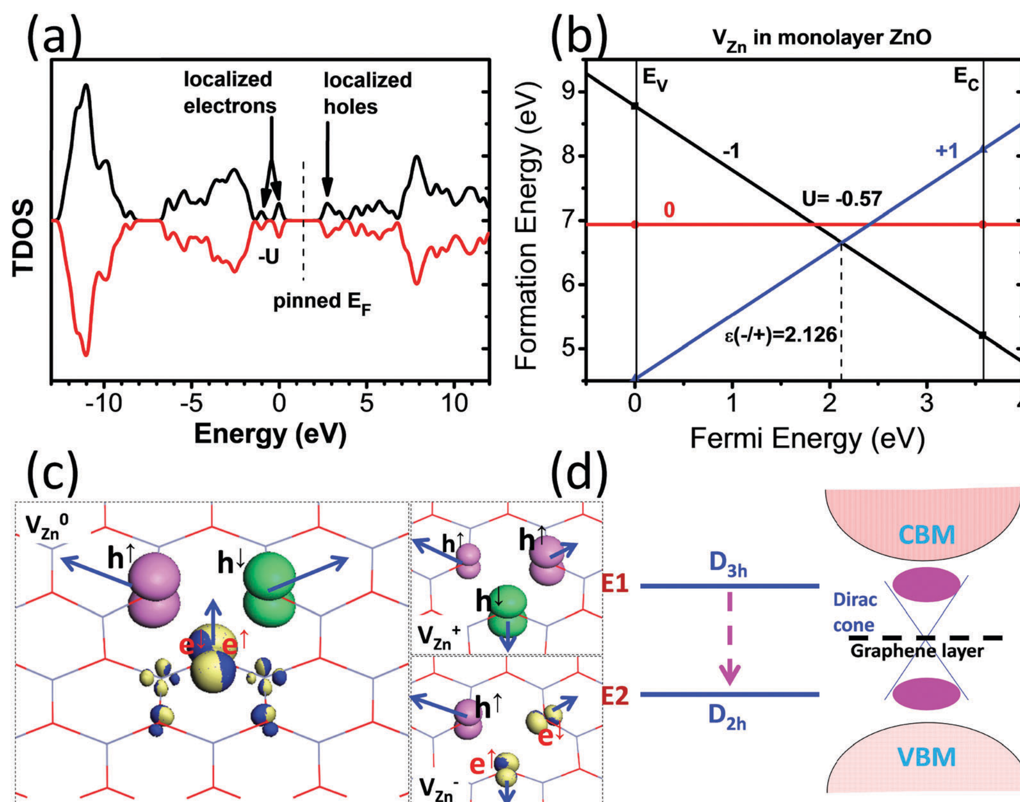

Fig. 6 (a) TDOS of the monolayer ZnO system with intrinsic neutral Zn vacancy (V_{Zn}^0). (b) Formation energy *vs.* Fermi energy within different charge states of 1−, 0, and 1+, for V_{Zn} in monolayer ZnO. (c) Localized orbitals electron and oxygen hole states near the valence and conduction band edges within charge states of 1−, 0, and 1+ (Zn = grey, O = red, spin-up hole state = pink, spin-down hole state = green, and spin-up and spin-down electrons = golden and blue). (d) Schematic diagram illustrating the decrease of energy as the symmetry is reduced from D_{3h} to D_{2h}, and the Dirac-cone levels pinned in the mid-gap of the host monolayer ZnO within the system of graphene/monolayer ZnO.

Open Access Article. Published on 19 April 2017. Downloaded on 9/18/2024 11:04:37 AM.
This article is licensed under a Creative Commons Attribution-NonCommercial 3.0 Unported Licence.

We also found that the hole and electron levels are not free-charge-carrier supply centers but are instead localized trap states. The intrinsic conductivity of monolayer ZnO may largely be restricted by such native defects. The E_F was actually pinned near the midgap. If we interface the system with a graphene layer, the position of the Dirac cone (cone apex level) will be pinned near the midgap of ZnO, owing to subtle electron–hole interactions (illustrated in Fig. 6(d)). This behavior can be understood by considering two extreme points in the CBM and VBM of the ZnO–graphene hybrid system. The electrons of the ZnO host lattice are delocalized, but the holes are bound and localized in the CB, while in the VB, the electrons are bound and the holes are freely delocalized. The Dirac cone apex level denotes the 2D free electron gas (from the graphene system) without the effective mass and presents the largest mobility, where electrons at that level are constrained in the graphene system. This means that in such 2D hybrid systems, competing interactions in the Coulomb potential are counteracted or balanced at the midgap where the cone level is located.

Additionally, Jahn–Teller distortion occurs in monolayer ZnO with V_{Zn} because the asymmetry between the occupancy of the p_{xy} and p_z orbitals within the planar monolayer ZnO is larger than that in non-centrosymmetric bulk WZ ZnO. This asymmetry can also be found in ZnO but is negligible.[95]

Doping limit in amorphous, 2D, and AABB ZnO

We further examined the amorphous and 2D monolayer ZnO systems. As seen in Fig. 7(a) and (b), the amorphous system has a doping range that is similar to that of WZ ZnO between the p- and n-type doping limit, which are 1.23 eV and 1.56 eV for amorphous and WZ ZnO, respectively. Remarkably, the p-type doping limit in the O-rich chemical potential of am-ZnO shifted

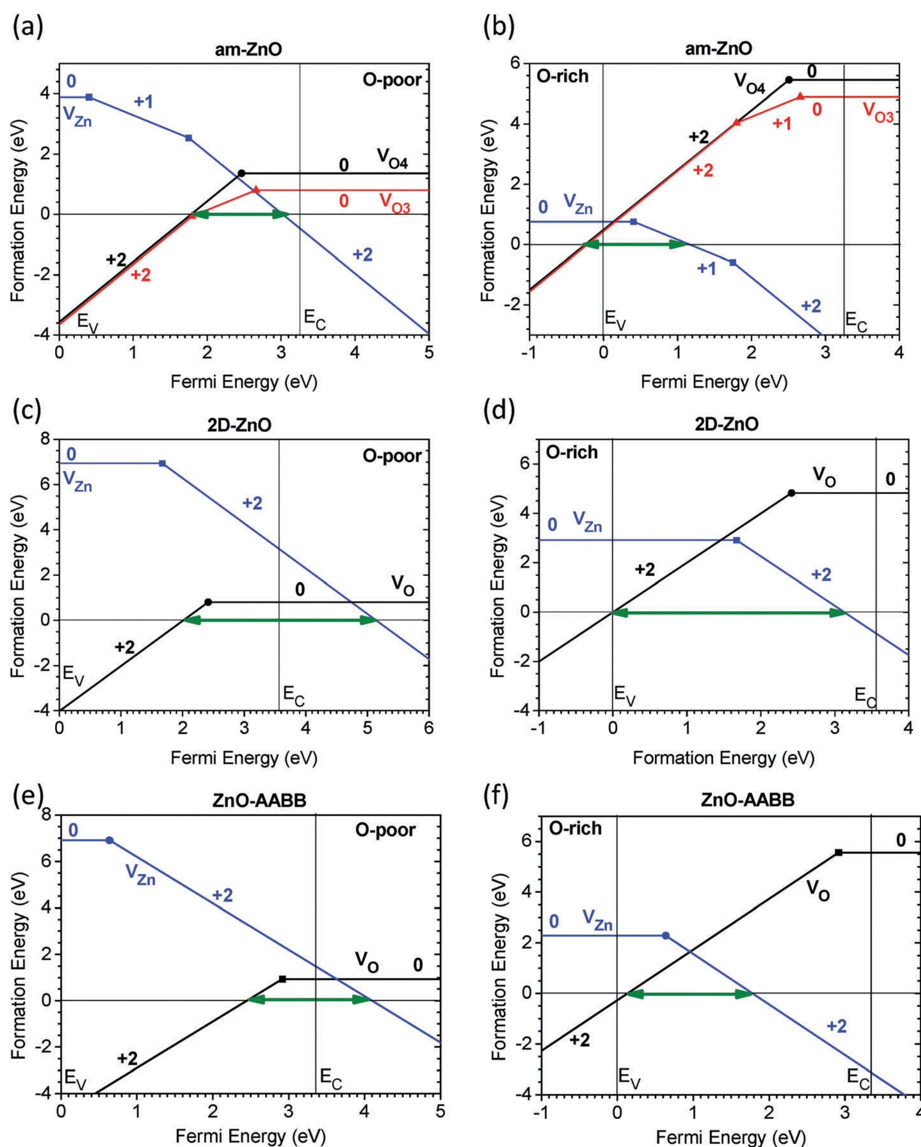

Fig. 7 Summary of doping limits of amorphous ZnO (a and b), 2D ZnO (c and d) and AABB ZnO (e and f) determined by the native point defects in both O-poor and O-rich limits, denoted by green arrows.

to the VB edge and overlapped with the E_F below the VBM. In the O-poor limit, the p-type doping limit is approximately E_V −0.26 eV (0.26 eV below the VBM), which is contributed by the positive doubly charged, 4-fold coordinated O vacancy (V_{O4}^{2+}) in am-ZnO. The only difference in the 3-fold coordinated O vacancy is in the formation energy at the neutral state in the O-poor limit, which is 1.36 eV and 0.80 eV for V_{O4}^{0} and V_{O3}^{0}, respectively. Though V_{O3}^{2+} is almost the same as V_{O4}^{2+}, V_{O3}^{2+} shows a positive U_{eff} with a value of U_{eff} = +0.86 eV, indicating the possibility of detection by ESR measurement. V_{O4}^{2+} has a relatively small negative U_{eff} of −0.13 eV, which is 20% of that of WZ ZnO. Thus, the amorphous structure not only possesses distorted Zn and O sites with randomly varied coordination but also reduces the Anderson-type effective spin correlation effect of multi-electrons at the same atomic site, leading to a reduced negative effective correlation energy ($-U_{eff}$) or even turning to the positive value.

V_{Zn}^{2-} has an n-type doping limit of 3.02 eV and 1.45 eV in the O-poor and O-rich limit, respectively. Note that the n-type doping limit in the O-poor limit deviated from the CB edge, showing lower n-type conductivity achieved by extrinsic donor dopants, such as Al_{Zn}. This indicates that am-ZnO can potentially easily adopt a p-type dopant under the O-rich limit, while still showing n-type dopable behavior under the O-poor limit because the n-type boundary overlaps with the CB. Therefore, am-ZnO has a bi-polar doping capability depending on the chemical potential limit, but the dopable range is relatively small compared to that of WZ-ZnO, due to the n-type limit shifting away from the CB.

Another important system is 2D ZnO, which consists of pure 3-fold coordinated Zn and O sites with a honeycomb lattice. As seen in Fig. 7(c) and (d), the dopable range increased from 1.56 eV to 3.13 eV. The variation in the doping limit under different chemical potential limits is very similar to the behavior of WZ ZnO. The p-type limit begins at E_V +2.01 eV and E_V +0 eV in the O-poor and O-rich limit, respectively, as determined by V_{O}^{2+}. The n-type doping limit was determined by V_{Zn}^{2-} and was E_V +5.14 eV and E_V +3.13 eV in the O-poor and O-rich limit, respectively. Our calculations show the physicochemical trend that 2D ZnO can undergo p-type doping. Moreover, an experimental study showed that a similar system can undergo both n- and p-type doping for flexible modulation of the doping behavior.[89]

From Fig. 7(e) and (f), AABB-type stacking in ZnO shows a similar doping limitation as that in the WZ lattice. In the O-poor limit, the E_F range without the spontaneous formation of native point defects spans from E_V +2.45 eV to E_V +4.10 eV. This range also overlaps with the CB, which is consistent with the conclusion that ZnO is an intrinsic n-type dopable solid system. In the O-rich limit, the dopable E_F range spans from E_V +0.13 eV to E_V +1.78 eV. This range is closer to the VBM than that calculated for the WZ system. However, this range still shows that this system has less flexibility for p-type doping than the am-ZnO and 2D ZnO systems discussed above. Thus, modulation of the 3D lattice stacking in bulk ZnO does not substantially improve the range to achieve p-type doping.

In contrast, GaN has a wide doping range, although it is also a wide-band-gap semiconductor like ZnO. GaN can be easily doped by both n-type and p-type dopants over its wide band gap area, while ZnO possesses asymmetric doping features, except in the 2D ZnO system. Most structures, such as WZ, ZB and am-ZnO, present only good overlap with the CB edge in the O-poor chemical limit, corresponding to the intrinsic n-type behavior of ZnO, and the E_F can be easily tuned by a donor dopant near the CB edge. However, the p-type limit shows that the E_F cannot be easily shifted towards or overlap the VB edge; thus, p-type doping is rather difficult to achieve in ZnO, as ZnO possesses an asymmetric dopable range according to the different chemical potential limits (Table 1).

Table 1 Summary of calculated bulk properties such as optical fundamental band gap, formation enthalpy, as well as O- and Zn-vacancy under different chemical potential limits in this work (unit: eV)

	Band gap	Formation enthalpy	V_{O}^{0} (O-poor)	V_{Zn}^{0} (O-rich)
WZ	3.444	−3.667	0.975	3.164
RS	3.883	−3.377	1.361	2.227
Am	3.250	−3.133	1.364/0.804	3.536
2D	3.570	−3.061	0.810	2.909

Wide selection and dopable range for rare earth (RE) ions in the 2D ZnO system

ZnO is a transparent semiconducting oxide with a wide band gap of 3.4 eV and can accommodate a wide range of RE ion dopants to modulate the output luminescence. Based on the above calculations and discussions, we found that the 2D 3-fold symmetrically arranged ZnO layered structure can adopt a relatively wide dopable range compared to the 3D bulk ZnO system. Therefore, it is highly desirable to conduct a preliminary theoretical study on RE ion doping and the related electronic states and properties. In this study, we mainly considered the RE^{2+} doping level. This study gives not only a theoretical reference for modulating the output luminescence *via* UC energy transfer but also theoretical guidance for future applications of low-dimensional, RE ion-doped, persistent phosphor luminescence materials.

We divided the RE elements doped in the ZnO system by their RE separation level: La, Ce, Pr, Nd, and Pm (radioactive) are the light RE elements; Sm, Eu, Gd, Tb, and Dy are the medium RE elements; and finally, Ho, Er, Tm Yb, and Lu are the heavy RE elements.

For the light RE elements, we first looked at the La-doped 2D ZnO system, as shown in Fig. 8(a). Substitution of the neutral La dopant at the Zn site (La_{Zn}^{0}) gives a localized electronic state with an s-orbital component near the CBM at E_V +3.0 eV (E_V denotes the position of the VBM). This accords with the fact that the $6s^2$ electrons in the valence orbitals of RE ions are the most easily ionized. The s-orbital electrons are donated into the system and aligned in a filled state below the CBM. Both the 5d and 4f states are above the CBM, and the CB in the system shows ferromagnetic (FM) spin alignment. The localized states are E_V +6.3 eV and E_V +7.2 eV, respectively. Doping with the singly positively charged species (La_{Zn}^{+}) induces AFM behavior, and E_V +6.0 eV and E_V +6.6 eV for the 5d and 4f empty states, respectively. Meanwhile, the top of the valence band of the ZnO host lattice is also slightly modified. For the doubly positively

Open Access Article. Published on 19 April 2017. Downloaded on 9/18/2024 11:04:37 AM.
This article is licensed under a Creative Commons Attribution-NonCommercial 3.0 Unported Licence.

Open Access Article. Published on 19 April 2017. Downloaded on 9/18/2024 11:04:37 AM.
This article is licensed under a Creative Commons Attribution-NonCommercial 3.0 Unported Licence.

Fig. 8 The projected partial density of states of light rare earth (RE) elements doped in 2D-ZnO layer structure (light RE: La, Ce, Pr, Nd, and Pm). (a) La_{Zn}, (b) Ce_{Zn}, (c) Pr_{Zn}, (d) Nd_{Zn} and (e) Pm_{Zn}.

charged doping state (La_{Zn}^{2+}), the localized hole state remains at E_V +0.3 eV above the VBM. The empty 5d and 4f levels produced by the La dopant slightly change to E_V +6.3 eV and E_V +6.9 eV, respectively. The top of the valence band is similar to that in the La_{Zn}^0 system but with slight FM behavior.

In the Ce-doped 2D ZnO system (Fig. 8(b)) at the Ce_{Zn}^0 doping state, the $6s^2$ electronic state occupies the E_F level (E_V +3.2 eV) below the CBM, and the 4f filled state is 0.2 eV below the E_F, or E_V +3.0 eV. The localized 4f empty states are at E_V +6.2 eV in spin-up configuration and at E_V +7.0 eV in spin-down configuration, showing FM spin alignment. The 5d empty states are nearly delocalized at E_V +6.8 eV and E_V +7.2 eV in the spin-up and spin-down configurations, respectively. For the Ce_{Zn}^+ state, the 4f filled state is localized at E_V +1.8 eV within the band gap of the ZnO host system and occupies the E_F of the whole system, and the level of the s-orbital is 0.4 eV above this E_F level. The 4f empty state in spin-up configuration is at E_V +5.1 eV, and in the spin-down configuration is at E_V +5.8 eV. The spin-up configuration of the 5d level is relatively more distinguishable and is found at E_V +5.9 eV. In the Ce_{Zn}^{2+} state, the system shows AFM behavior in the 4f and 5d spin alignments. The 4f states are all empty and localized at E_V +1.8 eV above the VBM, and the empty 5d levels are even higher at E_V +5.0 eV, approximately 1.5 eV above the CBM.

In the Pr-doped ZnO system, the neutral doping state (Pr_{Zn}^0) shows a localized 4f filled state at 1 eV above the VBM (E_V +1.0 eV) that is located near the midgap, as shown in Fig. 8(c). The E_F is also aligned with the s-orbital level. In the CB region, the localized 4f empty states have four levels with two spin-up orientations at E_V +5.7 eV and E_V +6.2 eV, while the spin-down levels are at E_V +7.4 eV and E_V +8.4 eV. The localized 5d empty states remain at E_V +6.5 eV and E_V +6.8 eV. The Pr_{Zn}^+ state of ZnO shows a localized

Open Access Article. Published on 19 April 2017. Downloaded on 9/18/2024 11:04:37 AM.
This article is licensed under a Creative Commons Attribution-NonCommercial 3.0 Unported Licence.

4f filled state 0.2 eV below the VBM (E_V −0.2 eV). The 4f empty states with spin-up configuration remain at E_V +4.5 eV and E_V +5.2 eV, while the spin-down states are at E_V +5.8 eV and E_V +6.3 eV. In the Pr^{2+}_{Zn} state, the 4f empty states are well distributed within the band gap of the host ZnO system. The spin-up configuration of the empty 4f localized levels remains at E_V +0.4 eV and E_V +0.7 eV, while the spin-down levels are localized at E_V +2.1 eV and E_V +3.2 eV. All of the localized 5d empty states are located at higher levels than the 4f orbitals, which remain at E_V +4.5 eV and E_V +5.1 eV.

In the Nd-doped 2D ZnO system, as shown in Fig. 8(d), the neutral state (Nd^{0}_{Zn}) shows a localized 4f filled state at 4.0 eV below the VBM (E_V −4.0 eV) that is buried within the valence band. As is known, the valence band mainly consists of O-2p orbitals of the ZnO system. The 4f empty states are 5.8 above the VBM (E_V +5.8 eV) in the spin-up configuration and at E_V +7.9 eV and E_V +9.0 eV in the spin-down configuration. The 5d empty states remain at E_V +6.3 eV and E_V +7.0 eV. For the Nd^{+}_{Zn} state, all of the 4f levels are shifted to lower energies. The filled 4f orbitals are at E_V −4.8 eV, while the empty 4f orbitals are at E_V +4.9 eV in the spin-up state and at E_V +7.1 eV and E_V +8.2 eV in the spin-down state. The 5d levels are localized at E_V +5.8 eV and E_V +6.2 eV. In the 2+ charge state of Nd_{Zn} doping (Nd^{2+}_{Zn}), a shallow hole state is localized at 0.2 eV above the VBM (E_V +0.2 eV), occupying the p-orbitals of O sites. The localized 4f filled level remains at E_V −4.8 eV below the VBM, which is almost unchanged from that of the 1+ state. The 4f empty states show a slight difference and are localized in the CB at E_V +5.2 eV in the spin-up configuration and at E_V +7.3 eV and E_V +8.4 eV in the spin-down configuration. The 5d empty levels accordingly remain at E_V +6.1 eV and E_V +6.5 eV.

The element Pm is radioactive. Although it is unsafe to actualize Pm-doping in ZnO, we still investigated the electronic properties of its doping in the 2D ZnO layered system, as shown in Fig. 8(e). In the Pm^{0}_{Zn} state, the 4f filled state is localized at E_V −5.3 eV below the VBM in the spin-up configuration. The corresponding empty states are localized at E_V +5.8 eV in the spin-up configuration and at E_V +8.6 eV and E_V +9.8 eV in the spin-down configuration. The 5d-orbital levels overlap with the 4f empty states at E_V +6.3 eV and E_V +7.2 eV. In its 1+ charge state (Pm^{+}_{Zn}), the 4f filled level shifts to E_V −6.3 eV. The 4f empty states are at E_V +4.8 eV in the spin-up configuration and at E_V +7.5 eV and E_V +8.6 eV in the spin-down configuration. The 5d levels are localized at E_V +5.7 eV and E_V +6.2 eV. For the 2+ charge state (Pm^{2+}_{Zn}), the 4f filled level is at E_V −6.1 eV. Similarly, the doping state produces a localized hole state at approximately 0.2 eV above the VBM, contributed by the p-orbitals. The 4f empty states remain at E_V +5.1 eV in the spin-up configuration and at E_V +7.8 eV and E_V +8.9 eV in the spin-down configuration. The localized 5d levels shift to E_V +6.0 eV and E_V +6.6 eV.

For the medium RE elements, Sm doping shows a behavior that is different from that of the light RE elements (Fig. 9(a)). In the neutral state (Sm^{0}_{Zn}), the 4f filled orbitals show a wider energetic range spanning from E_V −4.0 eV to E_V −6.0 eV, which overlaps with the O-2p orbitals. The empty states of the 4f orbitals remain at E_V +9.6 eV and E_V +10.6 eV in the spin-down configuration and are at E_V +5.5 eV in the spin-up configuration. The 5d orbitals of Sm^{0}_{Zn} remain at E_V +6.2 eV and E_V +7.5 eV. Sm^{+}_{Zn} doping gives 4f filled states localized below the VB, in contrast to the neutral state. The two peaks remain at E_V −5.3 eV and E_V −6.0 eV. The empty states of the 4f orbitals are located at E_V +4.6 eV in the spin-up configuration and at E_V +8.2 eV and E_V +9.5 eV in the spin-down configuration. The 5d orbitals are intermediate between the 4f empty states and are localized at E_V +5.5 eV and E_V +6.4 eV. For Sm^{2+}_{Zn} doping in the ZnO system, the 4f filled state is localized in the range of E_V −4.8 eV to E_V −6.5 eV. The shallow hole state is localized at 0.2 eV above the VBM in the spin-down configuration. The 4f empty state is 4.9 eV above the VBM in the spin-up configuration, while the spin-down states remain at 8.6 eV and 9.9 eV above the VBM. The spin-up and spin-down states of the 5d orbital are located at 5.8 eV and 6.8 eV above the VBM, respectively.

In Eu-doped ZnO, shown in Fig. 9(b), the 5d–4f level transition leads to red emission through dipole energy transfer. In the neutral state (Eu^{0}_{Zn}), the 4f filled state shifts higher than the VB of ZnO, indicating that the 4f occupied orbital levels are energetically higher than the 2p orbitals of the O sites in the host materials, which are at E_V +0.5 eV. In the singly positively charged state (Eu^{+}_{Zn}), the 4f filled states are below the VBM with a slight overlap, remaining at E_V −5.3 eV and E_V −6.2 eV. In the doubly positively charged state (Eu^{2+}_{Zn}), the 4f filled states are almost unchanged, where the empty states remain at E_V +2.8 eV and the lowest 5d level remains at E_V +5.3 eV. The energetic interval between the 4f empty state and the 5d state ranges from E_V +3.2 eV to E_V +5.2 eV, which affords red emission at 610 nm due to electronic de-excitation from $4f^{6}5d^{1}$ to $4f^{7}$.

With increased electronic occupation of the 4f orbitals, the 4f filled state of Gd further lowers and begins to overlap with the t_{2g} component of the $3d^{10}$ orbitals of the Zn sites, as shown in Fig. 9(c). Meanwhile, due to the repulsive Coulomb potential, the t_{2g} level of the $3d^{10}$ orbital shifts to a lower level compared to that in the undoped ZnO system. In this doping system, Gd^{0}_{Zn} contributes to the 4f filled state at E_V −7.2 eV below the VBM, while only one 4f empty state is present at E_V +8.2 eV above the VBM. The 5d levels occupy positions in the CB at E_V +6.2 eV and E_V +7.7 eV, showing FM behavior. In the Gd^{+}_{Zn} state, the 4f filled level overlaps with and is buried into the $3d^{10}$ orbitals of the Zn sites. This behavior arises because the positive charge state weakens the shielding effects of the valence shell of the Gd sites due to the reduced $6s^{2}$ environment, thus leading to a stronger repulsive interaction between the Gd-4f and O-2p orbitals and reaching E_V −8.2 eV. The 5d empty state is localized within the ZnO band gap at E_V +2.6 eV, and another two levels are located at E_V +5.3 eV and E_V +6.8 eV, overlapping with the CB of ZnO. The 4f empty state is found to be E_V +7.9 eV above the VBM. In the Gd^{2+}_{Zn} state, the behavior of the 4f filled state is similar to that of the singly positively charged state, but the level is raised by 0.4 eV to E_V −7.8 eV. Similarly, a localized shallow hole state results from the p-orbitals of the O sites of ZnO at 0.2 eV above the VBM. The localized 5d level in the band gap shifts to a higher energy of E_V +2.9 eV, and the other two levels remain

Open Access Article. Published on 19 April 2017. Downloaded on 9/18/2024 11:04:37 AM.
This article is licensed under a Creative Commons Attribution-NonCommercial 3.0 Unported Licence.

Fig. 9 The projected partial density of states of medium rare earth (RE) elements doped in 2D-ZnO layer structure (medium RE: Sm, Eu, Gd, Tb, and Dy). (a) Sm_{Zn}, (b) Eu_{Zn}, (c) Gd_{Zn}, (d) Tb_{Zn} and (e) Dy_{Zn}.

at E_V +5.6 eV and E_V +7.2 eV in the CBM. Meanwhile, the 4f empty state is also 0.3 eV higher (E_V +8.2 eV) than that in the Gd^{+}_{Zn} state.

The Tb-doping ZnO system (Fig. 9(d)) shows a different behavior from the Gd-doped system discussed above, especially in the 4f positions of both the filled and empty states. In the neutral doping state, Tb^{0}_{Zn} in ZnO leads to a 4f filled state localized within the valence band of ZnO contributed by the O-2p orbitals, which is E_V −3.3 eV below the VBM. However, this state does not contribute to the electronic transitions *via* energy transfer because parity selection forbids p–f transitions. Furthermore, other 5d and 4f filled states are also found to be localized within the band gap of ZnO at E_V +1.7 eV and E_V +2.2 eV in the spin-up and spin-down configuration, respectively. The 4f empty states overlap with the CB at E_V +6.5 eV and E_V +7.0 eV, both in the spin-down configuration. The 5d empty states remain high at E_V +7.7 eV, E_V +8.3 eV and E_V +9.8 eV. In the Tb^{+}_{Zn} doping state, the 4f filled state shifts lower to E_V −9.3 eV and overlaps with the $3d^{10}$ orbitals of the Zn sites. The E_F level is pinned at the VBM with a localized 5d-orbital contributed by the Tb site. The 4f empty state is localized near the midgap with an energy of E_V +1.5 eV. This behavior is completely different from that of the other medium RE elements but similar to that of the Ce-doped system. The 5d states are located at E_V +5.1 eV and E_V +7.0 eV in the CB. In the Tb^{2+}_{Zn} doping state, the 4f filled states are intermediate between the $3d^{10}$ and 2p orbitals, with twin peaks at E_V −6.2 eV and E_V −7.2 eV in the spin-up configuration. The E_F is also pinned near the VBM in the range of E_V to E_V +0.05 by two 4f orbital levels, one filled and the other empty. The filled 4f state remains at the VBM, and the empty 4f state is

Open Access Article. Published on 19 April 2017. Downloaded on 9/18/2024 11:04:37 AM.
This article is licensed under a Creative Commons Attribution-NonCommercial 3.0 Unported Licence.

hybridized with the neighboring O-2p orbitals, contributing a shallow hole level localized near the VBM. Therefore, Tb_{Zn}^{2+} in ZnO may be a good shallow acceptor. The empty states of the 4f orbitals remain near the CBM, with levels of E_V +2.8 eV and E_V +3.6 eV in spin-down alignment. The 5d levels are located at E_V +5.2 eV and E_V +6.6 eV.

In the Dy-doped system, as shown in Fig. 9(e), the 4f filled states are widely spread over the valence band and band gap, which is consistent with our previous work on the CaS system.[84] In the neutral state (Dy_{Zn}^{0}), the lowest two 4f filled states overlap with the bottom of the VB at E_V −4.2 eV and E_V −5.2 eV. The third 4f filled state occupies the VBM at 3.0 eV below the E_F level. The 5d filled level partially occupies the E_F level, while the empty state is located at E_V +6.2 eV. Meanwhile, the 4f empty states remain at E_V +7.0 eV and E_V +7.7 eV. For the Dy_{Zn}^{+} state, the lower three 4f filled states partially overlap with the O-2p orbitals at the bottom of the VB and remain at intermediate levels between the O-2p and Zn-3d orbitals at E_V −4.5 eV, E_V −5.6 eV and E_V −6.2 eV, all in the spin-up configuration. The highest occupied 4f orbital level is in the VB range at E_V −1.0 eV below the VBM in the spin-down configuration. The 5d levels remain in the gap at E_V +2.8 eV and in the CB at E_V +5.8 eV and E_V +6.7 eV. The 4f empty states are also in the CB at E_V +6.2 eV and E_V +7.2 eV in the spin-down configuration. For the Dy_{Zn}^{2+} doping state, the 4f filled levels are slightly different from those in the 1+ charge state, which are E_V −0.7 eV, E_V −4.2 eV, E_V −5.3 eV and E_V −5.9 eV below the VBM. A shallow hole state is localized on the p-orbital of the O sites at 0.3 eV above the VBM. The 5d level is localized at E_V +3.2 eV below the CBM. The higher energy levels are located at E_V +6.2 eV and E_V +7.1 eV in the CB. The 4f empty levels remain at E_V +6.5 eV and E_V +7.6 eV in the spin-down configuration.

We next examine the doping of heavy RE elements in ZnO, beginning with Ho (Fig. 10(a)). All the 4f filled states show the physical trend of lower energy levels resulting from increased 4f occupations. In the neutral state (Ho_{Zn}^{0}), the 4f filled states are located below the VBM, with one in the VB at E_V −3.0 eV and two between the Zn-3d and O-2p orbitals at E_V −5.3 eV and E_V −6.4 eV. The 4f empty state is localized at E_V +7.0 eV between the two localized 5d empty states, which are located at E_V +6.9 eV and E_V +7.8 eV. In the Ho_{Zn}^{+} doping state, the 4f filled states are localized at the lower energy levels of E_V −4.2 eV, E_V −6.5 eV, and E_V −7.6 eV. The 4f-emtpy states remain at E_V +5.6 eV and E_V +6.2 eV. The 5d empty states are localized at E_V +6.0 eV and E_V +6.8 eV. In the Ho_{Zn}^{2+} doping state, the 4f filled states are shifted to a slightly higher energy range and are located at E_V −3.9 eV, E_V −6.1 eV, and E_V −7.3 eV. The 4f empty states remain at E_V +6.0 eV and E_V +6.6 eV. The 5d orbitals are localized as empty states at E_V +6.5 eV and E_V +7.1 eV.

Er doping in ZnO provides interesting results, as shown in Fig. 10(b). In the neutral doping state (Er_{Zn}^{0}), the 4f filled states show similar behavior to those in the Ho-doped system. The filled levels are localized at E_V −1.3 eV, E_V −2.5 eV, and E_V −3.0 eV. For the empty states in the CB of ZnO, the 4f empty state is localized at E_V +8.8 eV in the CB, while the 5d states remain at E_V +6.8 eV and E_V +7.5 eV. For the Er_{Zn}^{+} doping state, the 4f filled states are shifted down to E_V −4.4 eV, E_V −6.0 eV, and E_V −7.1 eV. The 4f empty state is localized at E_V +7.6 eV. The 5d levels remain at E_V +6.0 eV and EV +6.5 eV. For the Er_{Zn}^{2+} doping state, the 4f filled states are even lower than the $3d^{10}$ level of Zn in the ZnO system and are localized at E_V −10.0 eV, E_V −12.4 eV, and E_V −13.6 eV. The 4f empty states are well localized within the band gap and range from EV +0.5 eV and EV +2.4 eV. The 5d states are also localized within the band gap at EV +0.4 eV above the VBM. Another three 5d states remain at EV +3.6 eV, EV +4.4 eV, and EV +5.6 eV. This doping state (Er_{Zn}^{2+}) may actualize NIR emission at a wavelength of approximately 654 nm (*i.e.*, photon energy of 1.9 eV). This energy transfer is primarily accomplished by the two localized d states within the band gap. As is known, the d–d transition is parity disallowed. However, the noncentrosymmetric local lattice of the RE dopant will relax the selection rule for electronic transitions. Fig. 10(b) shows the substantial p–d orbital overlap within the band gap at EV +0.4 eV above the VBM. At the same time, the ZnO lattice system possesses an inherent noncentrosymmetric atomic arrangement. Thus, electronic transitions under external photoirradiation, such as UV light, will occur resulting in higher level d orbitals at EV +3.6 eV. Upon overcoming the small energy barrier, the excited electrons can flip to a spin-down configuration (or the spin direction of the excited electrons can be reversed). Then, a triplet electronic de-excitation occurs between the higher energetic 5d level and the lower energy level of the 4f empty state. The direct minimum energetic interval of such de-excitation ranges from 1.7 eV to 1.9 eV, which is in good agreement with the experimentally suggested potential of the 654 nm NIR output emission.

The Tm-doped ZnO system, shown in Fig. 10(c), has no localized states within the band gap. In the neutral doping state (Tm_{Zn}^{0}), the 4f filled states largely overlap with the O-2p band (VB). The states are localized at E_V −3.4 eV, E_V −4.0 eV, E_V −4.5 eV, and E_V −5.7 eV. The 5d states are localized at EV +7.0 eV and EV +7.4 eV. The 4f empty state is localized at EV +7.3 eV. In the Tm_{Zn}^{+} state, the 4f filled states are localized below the VBM at E_V −5.2 eV, E_V −5.6 eV, and E_V −6.9 eV in the spin-up configuration and at E_V −3.6 eV, E_V −4.3 eV, and E_V −4.8 eV in the spin-down configuration. The 4f empty states remain at EV +6.2 eV, and the 5d states are localized at EV +6.3 eV and EV +6.6 eV. For the Tm_{Zn}^{2+} doping state, the localized states of the 4f and 5d orbitals are similar to those in the +1 charged state. The 4f filled states are localized at E_V −3.4 eV, E_V −4.2 eV, and E_V −4.6 eV in the spin-down configuration and at E_V −4.8 eV, E_V −5.3 eV and E_V −6.4 eV in the spin-up configuration. The shallow hole state is contributed by the distorted O sites occupying 2p orbitals at 0.2 eV above the VBM. The 4f empty state remains at EV +6.5 eV, and the 5d levels remain at EV +6.6 eV and EV +7.0 eV.

In Yb-doped ZnO (Fig. 10(d)), the 4f filled states are widely distributed within the valence band, which consists of O-2p orbitals, as seen in the neutral doping state (Yb_{Zn}^{0}). The CB shows FM spin alignment, and the E_F is pinned at the CBM, which is contributed by the s-orbitals of the Zn sites. The 4f empty state is localized at EV +5.0 eV, and the 5d levels are located at E_V +7.1 eV and EV +7.4 eV. In the 1+ charge state (Yb_{Zn}^{+}), the 4f filled states

Open Access Article. Published on 19 April 2017. Downloaded on 9/18/2024 11:04:37 AM.
This article is licensed under a Creative Commons Attribution-NonCommercial 3.0 Unported Licence.

Fig. 10 The projected partial density of states of heavy rare earth (RE) elements doped in 2D-ZnO layer structure (heavy RE: Ho, Er, Tm, Yb, and Lu). (a) Ho_{Zn}, (b) Er_{Zn}, (c) Tm_{Zn}, (d) Yb_{Zn} and (e) Lu_{Zn}.

are more localized than those in the neutral doping state and overlap with the O-2p orbitals. The 4f filled orbitals remain at E_V −2.2 eV and E_V −3.3 eV in the spin-down configuration and at E_V −3.9 eV, E_V −4.6 eV, and E_V −5.6 eV in the spin-up configuration. The 5d orbital levels are also localized in the gap at *EV* +2.8 eV, as well as at higher levels at *EV* +6.5 eV and *EV* +6.6 eV. The 4f empty state remains at *EV* +3.9 eV higher than the CBM. For the Yb_{Zn}^{2+} doping state, the 4f filled levels move to higher positions at E_V −2.0 eV and E_V −3.0 eV in the spin-down configuration and at E_V −3.4 eV, E_V −4.4 eV, and E_V −5.2 eV in the spin-up configuration. The shallow hole state is 0.3 eV higher than the VBM, occupying the O-2p orbitals. The 4f empty state remains at *EV* +4.2 eV, overlapping with the CB.

For the Lu-doped ZnO system (shown in Fig. 10(e)), the neutral doping state (Lu_{Zn}^{0}) produces a 4f filled state that is strongly localized near the bottom of the VB of ZnO at E_V −5.6 eV. Meanwhile, no localized 4f empty states are found in the ZnO system due to the $4f^{14}$ valence configuration of the Lu doping state. The 5d levels are located at *EV* +7.3 eV and *EV* +7.4 eV. The 4f filled state is lower in the Lu_{Zn}^{+} doping state and is located at E_V −6.8 eV. The 5d levels give two localized states at *EV* +2.8 eV below the CBM, while another two states are found in the CB at *EV* +6.7 eV. For the Lu_{Zn}^{2+} doping state, the 4f filled state shifts to E_V −6.6 eV. The 5d localized states in the gap are also shifted to *EV* +3.2 eV below the VBM, and another two states remain at *EV* +6.9 eV.

Thermodynamic transition levels of RE ions in the 2D ZnO system

The stability of the valence state of the doped RE ions in relation to the E_F position within the band gap area is significant and

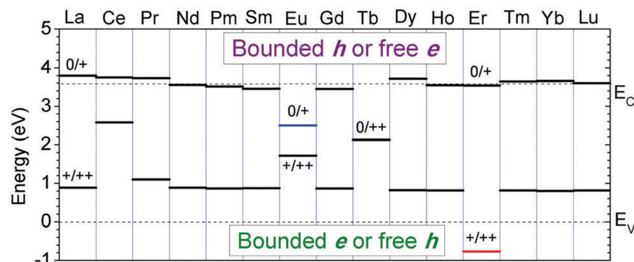

Fig. 11 Thermodynamic transition levels (TTL) of RE ions doped in the 2D-ZnO system by the charge state of 0, 1+, and 2+ for RE_{Zn} (RE = La,...,Lu).

can be determined by the TTLs, which is an important set of energy levels for measuring the zero-phonon line widths related to the CBM. As indicated in Fig. 11, most of the lanthanide elements in the RE_{Zn}-doped systems provide rather shallow donor levels close to the CBM or within the CB range at the (0/+) transition. However, the transition level for the (+/2+) state is a deep donor level, which hardly provides the mobile electrons necessary to ionize electrons with large energy barriers into the CB (E_C in Fig. 11). Most of the lanthanide substitutional dopants show positive U_{eff} features and can be detected on the surface of the sample using the ESR technique.

The Ce_{Zn} dopant is a relatively typical case in that its (+/2+) level is not as deep as that of other elements, while Tb_{Zn} has a negative U_{eff} of −0.1 eV with a deep (0/2+) transition level. This behavior clearly shows that the Tb_{Zn} dopant is not a donor source that provides freely mobile electrons in the ZnO lattice. Eu_{Zn} doping also gives deep donor levels. As shown by the blue line in Fig. 11, the (0/+) and (+/2+) transition levels remain at EV +2.50 eV and EV +1.72 eV, respectively. These deep levels can only trap electrons at the Eu_{Zn} site and may not ionize the electrons due to the large energy barrier below the CBM. Meanwhile, the single-particle calculation, shown in Fig. 9(b), indicates that Eu_{Zn}^{2+} may not be a red-emission center due to the $4f^65d^1$–$4f^7$ dipole transition, as the (0/+) level lies between the optical transitions and acts as an energy-depleting quench state.

More unusually, Er_{Zn} is found to be an extraordinary dopant with two contrasting (0/+) and (+/2+) TTLs. Er^+ in the 2D ZnO system is stable and energetically favorable throughout the entire band gap area with variations in the E_F. The (0/+) level is very shallow and aligns with the bottom of the CBM. Moreover, the TTL of the (+/2+) transition is found to be 0.76 eV below the VBM (or E_V −0.76 eV, E_V denotes the VBM), as shown in red in Fig. 11. As is known, the VB is the region in which bound valence electrons or delocalized energy transitions into free holes. This indicates that the (+/2+) transition produces free holes, and thus, Er^{2+} doped in the 2D ZnO system acts as a shallow acceptor center for capturing electrons or releasing free holes. This transition behavior may account for the experimentally reported enhanced NIR emission at 1540 nm induced by Er-doped ZnO nanomaterials.[96,97]

Excited states and relative oscillator strengths

The excited states in ZnO doped with different divalent lanthanide ions (Ln^{2+}, from La to Lu) were examined by a series of TD-DFT calculations, as shown in Fig. 12(a). These excitation energies correspond to the locations of the absorption peaks in the optical spectrum of a material and are more accurate than Kohn–Sham excitation energies. Some of the de-excitation paths between different energy levels correspond to the emission peaks from the output luminescence spectrum. The calculations were performed using the Tamm–Dankoff approximation.[98] This method allows us to calculate the full set of optical properties with the support of the excitation energies and the corresponding transition probabilities. This study is also applicable to low-dimensional ZnO systems, as extra effects such as boundary effects, quantum-confinement effects, and different coordination-induced mixed-valence effects are necessarily taken into account.

Fig. 12(b) shows the excited state energy levels of trivalent lanthanide ions doped within the bulk ZnO host lattice. In contrast to the divalent ion-doped systems, the excited state energy levels are mostly distributed within the band gap area, especially in the lower energy range (<2.0 eV). This behavior indicates that Ln^{3+} ions have a much wider absorption window in the NIR excitation range than Ln^{2+} ions, as most of the Ln^{2+} excited state levels are near the CBM of the host ZnO with excitation energy near the band gap of ZnO (∼3.4 eV), as shown in Fig. 12(a).

Notably, Dorenbos *et al.* examined divalent and trivalent states of lanthanide elements doped in a crystal host (*e.g.*, ZnO) and determined the minimum energy levels of the excited states.[99–102] This examination of energy levels provides a significant starting point for further examination of energy transfer between different lanthanide ions, especially in the case of co-doping.

Meanwhile, it is helpful to consider the work-function or position relative to the vacuum level of a multi-faceted, low-dimensional ZnO nanomaterial system exposed to vacuum. This model is more realistic for the study of UC luminescence energy transfer in nanoparticles or nanocrystals. The calculations in this study are based on the bulk system, since the energy transfer mechanism and photoelectronic dynamics related to intrinsic defects or extrinsic dopants are still not very clear. Thus, we first examine the bulk system and then plan to extend our computational approach to other low-dimensional ZnO systems in the following studies.

Valence states of Ln ions doped in ZnO

We also considered Ln ions with mixed valences doped in ZnO. It is synthetically possible to produce mixed valence states of Ln ions between Ln^{2+} and Ln^{3+}. These states may have different transition behaviors between excited state energy levels compared to the single-valence Ln^{2+} or Ln^{3+} ionic states. Here, we introduce that the excited state energy levels computed by TD-DFT together with the oscillator strength can be used to distinguish the different contributions to luminescence from the excited state energy level transitions. The relative oscillator strength determines the intensity of the absorption and emission by an external excitation source. Meanwhile, the relative oscillator strength illustrates the probability of transitions for the excited electrons and the kinetic rate constant for transitions among the different levels.

Open Access Article. Published on 19 April 2017. Downloaded on 9/18/2024 11:04:37 AM.
This article is licensed under a Creative Commons Attribution-NonCommercial 3.0 Unported Licence.

Open Access Article. Published on 19 April 2017. Downloaded on 9/18/2024 11:04:37 AM.
This article is licensed under a Creative Commons Attribution-NonCommercial 3.0 Unported Licence.

(a)

Energy (eV)

7.5
7.0
6.5
6.0
5.5
5.0
4.5
4.0
3.5
3.0
2.5
2.0
1.5
1.0
0.5
0.0
-0.5
-1.0

E_C

E_V

La Ce Pr Nd Pm Sm Eu Gd Tb Dy Ho Er Tm Yb Lu

Open Access Article. Published on 19 April 2017. Downloaded on 9/18/2024 11:04:37 AM.
This article is licensed under a Creative Commons Attribution-NonCommercial 3.0 Unported Licence.

(b)

Energy (eV)

8.0 7.5 7.0 6.5 6.0 5.5 5.0 4.5 4.0 3.5 3.0 2.5 2.0 1.5 1.0 0.5 0.0 -0.5 -1.0

E_C

E_V

La Ce Pr Nd Pm Sm Eu Gd Tb Dy Ho Er Tm Yb Lu

Open Access Article. Published on 19 April 2017. Downloaded on 9/18/2024 11:04:37 AM.
This article is licensed under a Creative Commons Attribution-NonCommercial 3.0 Unported Licence.

(c)

La
Ce
Pr
Nd
Pm
Sm
Eu
Gd
Tb
Dy
Ho
Er
Tm
Yb
Lu

Relative Oscillator Strength

Energy (eV)

(d)

La Ce Pr Nd Pm Sm Eu Gd Tb Dy Ho Er Tm Yb Lu

Relative Oscillator Strength

Energy (eV)

Open Access Article. Published on 19 April 2017. Downloaded on 9/18/2024 11:04:37 AM.
This article is licensed under a Creative Commons Attribution-NonCommercial 3.0 Unported Licence.

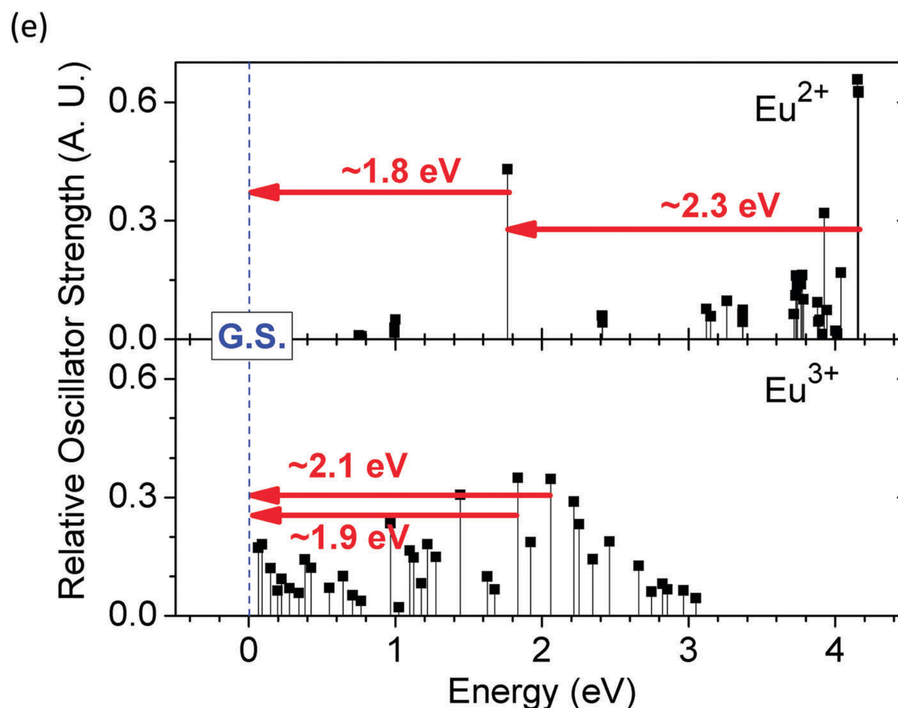

Fig. 12 (a) Excited state levels for Ln^{2+} doping ions in ZnO. (b) Excited state levels for Ln^{3+} doping ions in ZnO. (c) The oscillator strength for each corresponding excited state of the Ln^{2+} doping ion. (d) The oscillator strength for each corresponding excited state of the Ln^{3+} doping ion. (e) The calculated oscillator strengths for Eu^{2+} and Eu^{3+} doping in ZnO are shown for comparison (G.S. denotes the ground state level located at 0 eV).

Open Access Article. Published on 19 April 2017. Downloaded on 9/18/2024 11:04:37 AM.
This article is licensed under a Creative Commons Attribution-NonCommercial 3.0 Unported Licence.

Following the above discussion, we extracted the optical matrix elements from the calculations and converted them into relative oscillator strengths (transition probabilities) to discuss the probabilities of energy transfer as well as the lifetime of excited electrons at the specific level. The relative oscillator strength for each excited energy level is demonstrated in Fig. 12(c) and (d) for both Ln^{2+} and Ln^{3+} in the bulk ZnO lattice. In some cases, these excited state energy levels are dominated by contributions from the Russell–Saunders term $^{2S+1}L_J$, and the presentation of ladder-like energy levels is similar to the work of Dieke[103] or Carnall *et al.*[104] However, in most cases, the crystal-field splitting components, which contribute $4f^N$ fine levels, are evident and rather dense in the energetic intervals,[105] as shown in Fig. 12(a) and (b), which is in agreement with the work of Morrison *et al.*[106] Here, in the wavefunctions, we account for all the effects of the energetic differences of the valence electrons with different behaviors. The physicochemical trend of the energy excitations of the electrons follows a similar trend as seen in the work of Carnall *et al.*[104] Some deviations can be attributed to the bonding in ZnO, which is not a fully ionic crystal, such as LaF_3, and contains partially covalent bonding features.

As shown in Fig. 12(e), Eu-doped ZnO can output red emission with a wavelength of approximately 650 nm (or 1.9 eV photon energy). In our calculated excited state, approximately 1.80 eV is necessary for the excited electron to de-excite back to the ground state. However, intermediate low energy states at approximately 1.0 eV may act as energy depletion paths to reduce the intensity of the emission, even though the oscillator strength is as small as 0.01. Meanwhile, as our thermodynamic transition levels illustrated, the deep transition levels of Eu-doped ZnO are unlikely to maintain the Eu^{2+} charge state in the energetic range of optical transitions near the midgap. Therefore, Eu_{Zn}^{2+} in the ZnO system may not be a highly efficient NIR/red luminescence center within the wavelength range of the first biological window. This corresponds to the experimental report that stated that the existence of Eu^{3+} in ZnO is actually responsible for the red luminescence.[107,108] Meanwhile, the higher energy emission at 590 nm (2.1 eV), which was reported experimentally,[35] that neighbors the Eu-intrinsic de-excitation at 615–650 nm is rather low and could be viewed as having zero oscillator strength, as shown in Fig. 12(e). Theoretically, both Eu^{2+} and Eu^{3+} can account for the observed red emission in ZnO, showing a similar trend as a recent experimental report.[109] The probability analysis (oscillator strengths) of the divalent and trivalent states of Eu shows that two different energy transfer mechanisms can lead to red luminescence. Eu^{2+} shows two de-excitations from higher lying excited states back to the lower $^5D_0$ level, followed by the second transition of $^5D_0$ back to $^7F_0$. For Eu^{3+}, the electrons at two different excited states are de-excited back to the ground state, as shown in Fig. 12(e).

How can we further distinguish the real valence state of Eu ions doped in the ZnO system? Using TD-DFT calculations, we confirm that the transitions of Eu excitation levels in ZnO can be distinguished through differences in the luminescence intensity. According to the experimental observation by Hao *et al.*,[35] longer wavelength emissions are always more intense in Eu-doped ZnO systems. As shown in Fig. 12(e), Eu^{2+} has a higher probability for energy transfer at larger energetic intervals.

Open Access Article. Published on 19 April 2017. Downloaded on 9/18/2024 11:04:37 AM.
This article is licensed under a Creative Commons Attribution-NonCommercial 3.0 Unported Licence.

Thus, the divalent state of Eu does not act as the dominant red-emission center. Meanwhile, the mechanism for emission at 600 nm is unlikely to be the sole de-excitation from UC among the excited states. Indeed, red emission is supported by inter-defect-level transitions among the zero-phonon lines (with negative U_{eff}), leading to enhanced luminescence.[51]

Er doped in ZnO has been experimentally reported to generate NIR output luminescence at approximately 1540 nm (0.8 eV photon energy).[110] In the Er^{2+} excited levels shown in Fig. 12(a), de-excitation from the first excited state back to the ground state (0 eV) may correspond to the luminescence energetic output with an interval of 0.81 eV (1530 nm wavelength). For the Er^{3+} excited states, the output may result from a transition from the second excited state back to the first excited state with an interval of 0.52 eV, which is slightly larger than the Er^{2+} emission wavelength. However, in the medium energetic scale, Er-doped ZnO outputs green emission, showing twin peaks from 525 nm to 560 nm.[110] As shown in Fig. 12(a) and (b), Er^{2+} and Er^{3+} both contribute to energy transitions, with Er^{3+} showing a slightly higher oscillator strength. Therefore, luminescence in ZnO due to Er doping probably has a mixed valence state between 2+ and 3+ or potentially exhibits a valence state transition resulting from different external excitations, such as different injection currents or voltages *via* the electroluminescence (EL) technique.[110]

Er doping in wide-band-gap, group III–V semiconductors has been studied at low temperature, and emission at 1540 nm has been reported to result from transitions from the first excited spin–orbit state $^4I_{13/2}$ to the $^4I_{15/2}$ ground state of Er^{3+} ($4f^{11}$). However, so far, there is no conclusive evidence of the lattice site of luminescent Er ions in a specific valence state.[111] The (Er,Tm) co-doping of ZnO has also shown that emission at 1540 nm can be observed by Er and Tm individually, which indicates that the energy scale allows for intrinsic transitions of Tm ions doped in the ZnO lattice.[112] As seen in Fig. 12(c) and (d), Tm^{2+} ions lead to very small energy splitting between the spin–orbit transition from $^3F_4$ to $^3H_6$, while Tm^{3+} ions undergo a transition with similar energy and a relatively high oscillator strength. For emission in the shorter wavelength range, the Tm-doped ZnO thin film can achieve the observed blue (480 nm) and red (800 nm) emissions *via* the electroluminescence (EL) technique, using a higher injection current and voltage.[110] As shown in Fig. 12(c), there are two distinctly high oscillator strengths below 3.0 eV at approximately 1.61 eV and 2.60 eV. Therefore, Tm^{3+} in ZnO is responsible for the long-wavelength NIR emissions at 1540 nm and 1800 nm,[112] while Tm^{2+} in ZnO can account for the emissions at 480 nm and 800 nm generated by the electroluminescence (EL) technique.[110]

Energy transport and modulation

We summarized the oscillator strength and the corresponding excited state energy levels of all 15 lanthanide ions in the 2+ and 3+ charge states, as shown in Fig. 13(a) and (b), respectively. In the Ln^{2+} doping state (Fig. 13(a)), energy transitions at the CBM edge absorption or higher ($\sim$3.4 eV or $>$3.4 eV) predominate medium and heavy lanthanide ions. The light lanthanide elements have excited state energy transition levels within the band gap with lower oscillator strength compared to the medium or heavy lanthanides.

However, the situation is clearly different for the Ln^{3+} doping state (Fig. 13(b)). The oscillator strengths of all lanthanide ions are reduced, and the excited state energy levels are shifted to below 3.0 eV. This phenomenon is very similar to a famous concept in biology called the removal of apical dominance. This concept is usually observed in living plants, in which the apex of the plant has a rather strong tendency to grow, resulting in inhibited development of the lower branches. This originates from unbalanced plant food absorption, which is stronger at the top apex than in the branches. Continuous energy harvesting induces transportation paths for growth auxins (or phytohormones), which is the main cause of inhibition. Manually removing the apex will stop energy transport to the top and shift it to the lower branches so that the living plant can achieve wider plant growth. Analogous to energy transport and conversion in Ln-doped UCNPs, Ln^{3+} ions, as the sensitizing dopant, reduce the energy barrier for excited state absorption, showing wider energy transfer channels that are evenly distributed within 3.0 eV, which is lower than the CB edge absorption in Ln^{2+}-doped ZnO. Meanwhile, each energy level has a stronger oscillator strength, indicating a larger probability for excitation and energy transport between the inter-levels. This phenomenon for trivalent Ln doping, in physicochemical and biological terms, follows the removal of apical dominance concept, leading to more flexible energy transfer within the biological window.

Further details are shown in Fig. 13(c) and (d) in a 3D view. The higher energy transitions from Ln^{2+} to Ln^{3+} are not suppressed by forbidden transitions or real quenching effects induced by different trap levels. Instead, the inhibition results from competition among the various kinetic reaction rate constants of the lanthanide dopant ions. Yan *et al.* provided a similar discussion of the rate constant competition and transfer by studying the UC luminescence of a $NaYF_4$@CaF_2(Er,Yb) core@shell system.[113,114]

Finally, to design an optimal transmission channel for energy transfer among sensitizer and activator ions, as well as energy transport through the lattice, the oscillator strength and excited state energy levels must be comprehensively considered. Proper transfer and transport require not only a large probability (oscillator strength) of transition between excited state levels but also a wide and even distribution of these levels that largely overlaps with the intrinsic band structure of the host. Meanwhile, the conventional view of 4f-dominated transitions among excited states is no longer universally accepted to interpret different energy transfers of UC luminescence, which may restrict the future synthesis of novel nanoparticles with easily modulated output luminescence. Actually, d–f hybrid transitions of the lanthanide doping ions within various systems can contribute different charge-transfer-induced energy migrations between the excited states of different ions,[115] which is potentially useful to support energy transfer for self-sensitization, such as that for a rather wide-band-gap host lattice at 654 nm (1.89 eV photon energy).[116]

To establish a correlation between the excited energy levels and the corresponding oscillator strengths, we summarized

Open Access Article. Published on 19 April 2017. Downloaded on 9/18/2024 11:04:37 AM.
This article is licensed under a Creative Commons Attribution-NonCommercial 3.0 Unported Licence.

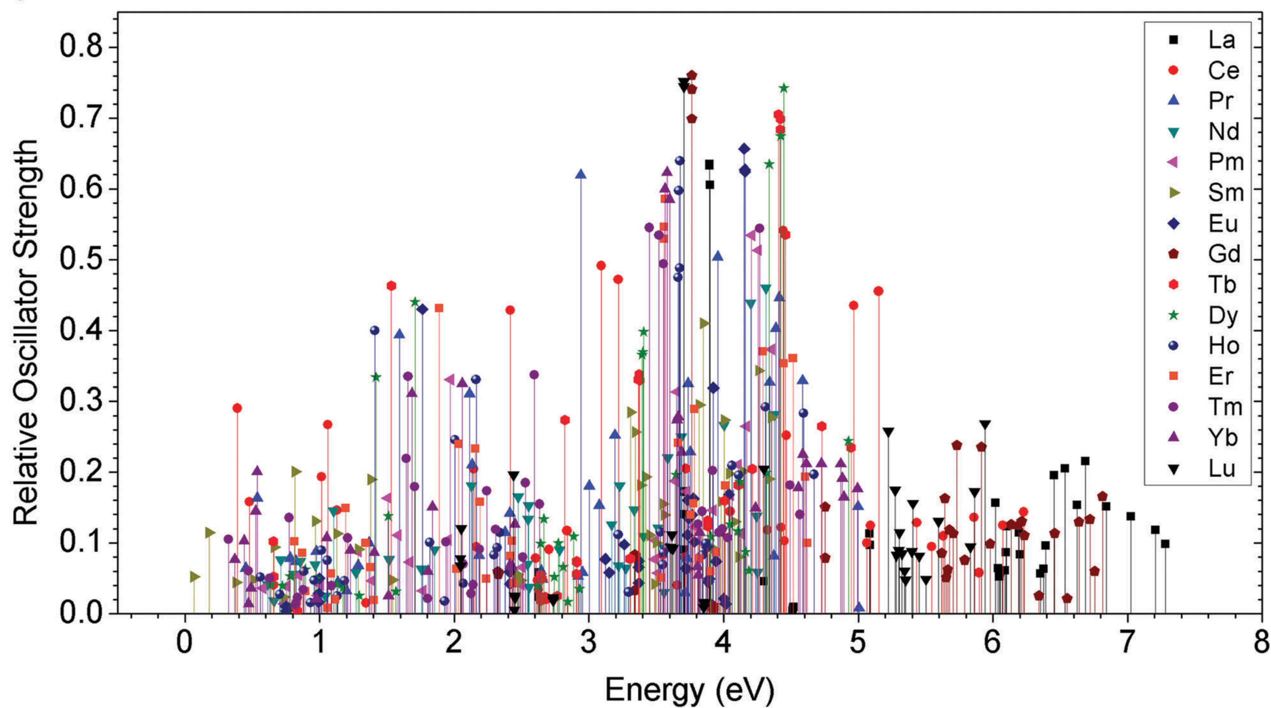

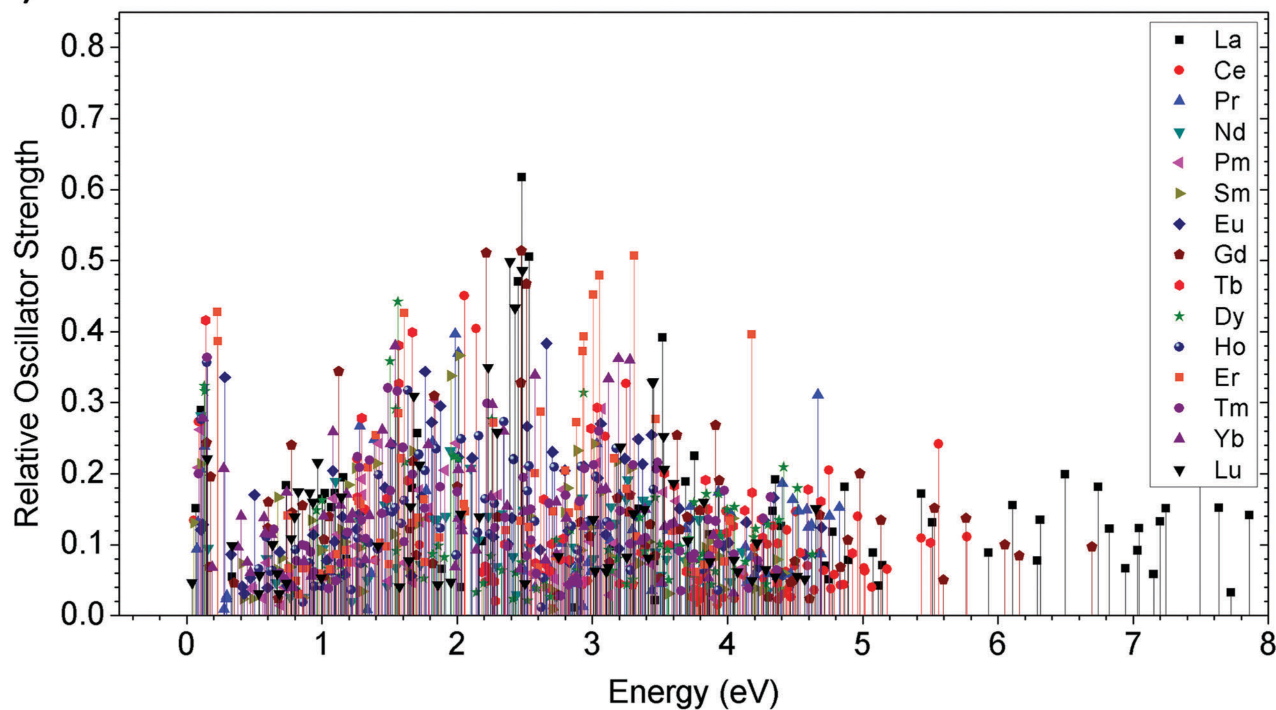

Open Access Article. Published on 19 April 2017. Downloaded on 9/18/2024 11:04:37 AM.
This article is licensed under a Creative Commons Attribution-NonCommercial 3.0 Unported Licence.

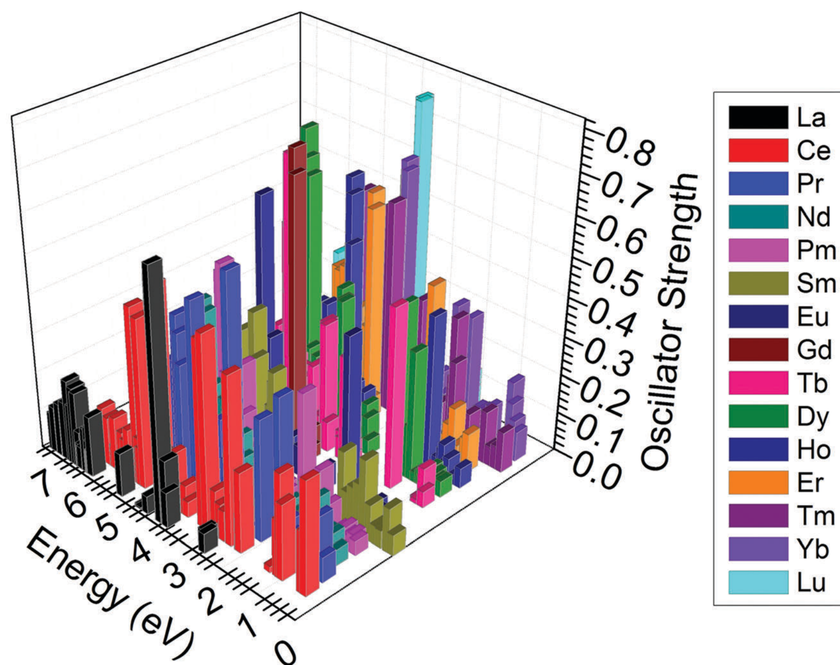

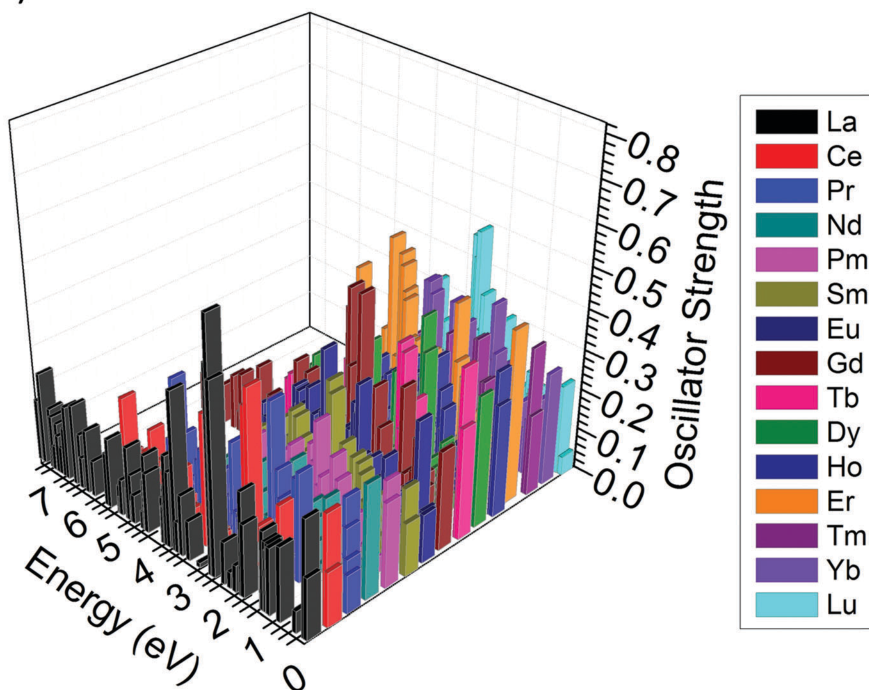

Open Access Article. Published on 19 April 2017. Downloaded on 9/18/2024 11:04:37 AM.
This article is licensed under a Creative Commons Attribution-NonCommercial 3.0 Unported Licence.

Fig. 13 (a) The relative oscillator strength for each corresponding excited state is shown by the 15 lanthanide doping ions within the bulk ZnO lattice. The levels of divalent ions and trivalent ions are shown in (a) and (b), respectively. The summary of the relationship between oscillator strength and excited state energy level is shown in 3-dimensions (3D) with Ln^{2+} (c) and Ln^{3+} (d). The Smith-charts illustrate a range of 15 lanthanide dopant ions in ZnO for modulating the output emission luminescence properties, where the Ln^{2+} ions are shown in (e) and Ln^{3+} are shown in (f).

Open Access Article. Published on 19 April 2017. Downloaded on 9/18/2024 11:04:37 AM. This article is licensed under a Creative Commons Attribution-NonCommercial 3.0 Unported Licence.

these parameters in a Smith chart to understand the overarching relationships. The horizontal direction gives the excited energy levels, while the vertical direction shows the oscillator strength. We approximated the lifetime and cross-relaxation into a phase difference *via* an exponential decay function to give an overall graphical view of the potential high-efficiency energy transfer in UC luminescence materials composed of lanthanide-doped ZnO.

In addition, the Smith chart in Fig. 13(e) illustrates that heavy lanthanide elements usually dominate the energy transmission channel at high energy, medium lanthanide elements mostly occupy the middle range of the optical fundamental gap, and light lanthanide elements are widely spread over the optical band gap, as well as over the partial CB range.

However, as shown in Fig. 13(f), following the removal of apical dominance concept, Ln^{3+} shows wider distributed energy transfer channels within 3.0 eV, contributing a more flexible biological window for *in vivo* imaging or other related opto-electronic devices.

Lifetime and decay time

The emission time for luminescence materials can be divided into two ranges depending on the length and mechanism: fluorescence and phosphorescence. Persistent luminescence is an optical phenomenon attributed to phosphorescence persisting for several seconds to hours or even days.

The lifetime τ is an important parameter for describing the fluorescence resulting from inter-level transitions between excited states. For emission, $\tau \propto 1/(\omega^3 D^2)$, where ω is the photon frequency (*i.e.*, photon energy is $\hbar\omega$) and D is the dipole moment. In another description following the Lorentz local field under the vacuum cavity model framework, the lifetime is correlated to the oscillator strength: $\tau \sim (1/f)[9n\lambda_0(n^2+2)^2]$, where f is approximated by the electric-dipole transition, λ_0 is the emission wavelength and n is the refraction index of the luminescence sample.[117]

However, the situation is different for persistent luminescence (phosphorescence). The lifetime τ for the fluorescent is no longer effectively described the persistent luminescence. As Leverenz summarized,[118,119] excited electrons are trapped by intrinsic defects or extrinsic impurities in the host, and most of these trap depths are evidently distant from the delocalized states near the CB edge. Therefore, the luminescence time is described by the exponential decay function $I = I_0\exp(-at)$, which is independent of the luminescence temperature, *via* the power law $I = I_0 t^{-n}$, but dependent on the phosphor temperature. Our recent work was consistent with the Leverenz model in that energy transfer in persistent luminescence is likely independent of the temperature but is strongly correlated with electron-lattice coupling in the defect states.[51] Currently, no universal analytic theoretical equations for the decay time exist; however, the decay time can be expressed by an effective multi-center emission approximation with consideration of the thermal effects as follows:

$$I(t) = I_{01}\exp[-\nu_1 t\exp(-\Delta E_1/k_BT)] + I_{02}\exp[-\nu_2 t\exp(-\Delta E_2/k_BT)] + \cdots + I_{0N}\exp[-\nu_N t\exp(-\Delta E_N/k_BT)], \quad (2)$$

where the subscripts 1, 2,...,N denote the different trap centers contributed from intrinsic defects or extrinsic doping impurities, ΔE_N represents the trap depth relative to the CBM for the Nth trap center, and I_{0N} is the ideal emission output intensity at time $t = 0$.

In this work, as shown in Fig. 8–10, the calculated single-particle levels determine the trap depth of each lanthanide dopant, which describes its contribution to the persistent luminescence of ZnO. Meanwhile, these localized electron and hole states also reduce the energy barrier for bound electrons to transfer from the VBM to the CBM directly from the host lattice. If we choose a lanthanide element as the first dopant to act as a luminescence center (*i.e.*, activator), then a suitable secondary dopant must be determined to extend the lifetime.

As shown in Fig. 8, among the light lanthanide elements, Ce and Pr are suitable candidates for extending the persistent luminescence lifetime (or decay time) because Ce and Pr have relatively low electron trap levels, which are low-lying in the optical band gap. As noted in eqn (2), the deeper the trap depth, the longer the decay time of persistent luminescence. Among the medium lanthanide elements, as shown in Fig. 9, Eu, Tb, and Dy are suitable secondary dopants to prolong the decay time *via* extending the trap depth to even deeper positions, particularly the dopant Dy. Previous studies have confirmed that Dy is a suitable secondary dopant for the temporal extension of persistent luminescence.[84,120,121] Among the heavy lanthanide elements, as shown in Fig. 10, no suitable candidates provide electronic trap levels far enough away from the CBM. Thus, among all the lanthanide elements, Dy is the best secondary dopant for the persistent luminescence of ZnO nanomaterials. Note that this deduction is only valid based on the trap-depth model by Leverenz. Further theoretical analysis of the decay time of persistent luminescence will be explored in future work.

Summary

The doping limits in various ZnO structures were determined by their native point defect formation energies. Chemical trends of the doping limits of ZnO were shown by comparing the formation energy and the E_F in terms of doping pinning limit energies. Furthermore, the doping limits and corrected electronic properties were examined for an amorphous solid ZnO material. We found that the am-ZnO system is p-type dopable with acceptor dopants, since its p-type pinning energy overlaps with the VB edge. However, p-type doping is achieved at the cost of lower electronic affinities of various Zn- or O-sites, indicating a potential loss of the n-type behavior of ZnO. The 2D ZnO system expands the doping limit range from the VB to the CB edge, indicating that 2D ZnO is a promising low-dimensional nanomaterial. This material not only lowers the coordinate numbers of the Zn and O sites, which lowers the electron affinity, but also shifts the charge neutrality level towards the lower part of the band gap close to the VB edge.

To further our examination of energy transfer in UC luminescence by RE ion doping, the excited state levels were extensively

studied for all 15 lanthanide (Ln) elements in both the Ln^{2+} and Ln^{3+} ionic charge state. We also considered the probability of mixed valences of the Ln dopant ions occurring in ZnO and analyzed the relative oscillator strengths to discuss the transition probabilities for energy transfer by excited electrons at the specific level. We found that at the Ln^{2+} charge state, heavy lanthanide elements usually dominate the energy transmission channel at high energy, medium lanthanide elements mostly occupy the middle range of the optical fundamental gap, and light lanthanide elements are widely spread over the optical band gap as well as over the partial CB range. However, at the Ln^{3+} charge state, following the removal of apical dominance concept, Ln^{3+} has wider distributed energy transfer channels within 3.0 eV, which contributes a more flexible biological window for *in vivo* imaging or other related optoelectronic devices.

Acknowledgements

This work is supported by the Natural Science Foundation of China (NSFC) for the Young Scientist grant (Grant No. NSFC 11504309), the initial start-up grant support from the Department General Research Fund (Dept. GRF) from ABCT at Hong Kong Polytechnic University, and the Early Career Scheme (ECS) Fund (Grant No. PolyU 253026/16P) from the Research Grant Council (RGC) in Hong Kong.

References

1 Ü. Özgür, Y. I. Alivov, C. Liu, A. Teke, M. A. Reshchikov, S. Doğan, V. Avrutin, S.-J. Cho and H. Morkoç, *J. Appl. Phys.*, 2005, **98**, 041301.
2 K. Hiruma, M. Yazawa, T. Katsuyama, K. Ogawa, K. Haraguchi, M. Koguchi and H. Kakibayashi, *J. Appl. Phys.*, 1995, **77**, 447.
3 J. Hu, T. W. Odom and C. M. Lieber, *Acc. Chem. Res.*, 1999, **32**, 435.
4 Z. W. Pan, Z. R. Dai and Z. L. Wang, *Science*, 2001, **291**, 1947.
5 M. H. Huang, S. Mao, H. Feick, H. Yan, Y. Wu, H. Kind, E. Weber, R. Russo and P. Yang, *Science*, 2001, **292**, 1897.
6 M. Law, L. E. Greene, J. C. Johnson, R. Saykally and P. Yang, *Nat. Mater.*, 2005, **4**, 455.
7 J. J. Cole, X. Wang, R. J. Knuesel and H. O. Jacobs, *Nano Lett.*, 2008, **8**, 1477.
8 H. Cao, J. Y. Xu, D. Z. Zhang, S. H. Chang, S. T. Ho, E. W. Seelig, X. Liu and R. P. H. Chang, *Phys. Rev. Lett.*, 2000, **84**, 5584.
9 H. Cao, J. Y. Xu, E. W. Seelig and R. P. H. Chang, *Appl. Phys. Lett.*, 2000, **76**, 2997.
10 H.-M. Xiong, *Adv. Mater.*, 2013, **25**, 5329.
11 C. Zhang, F. Zhang, T. Xia, N. Kumar, J.-i. Hahm, J. Liu, Z. L. Wang and J. Xu, *Opt. Express*, 2009, **17**, 7893.
12 J. E. Stehr, S. L. Chen, N. K. Reddy, C. W. Tu, W. M. Chen and I. A. Buyanova, *Adv. Funct. Mater.*, 2014, **24**, 3760.
13 F. Auzel, *Chem. Rev.*, 2004, **104**, 139.
14 F. van de Rijke, H. Zijlmans, S. Li, T. Vail, A. K. Raap, R. S. Niedbala and H. J. Tanke, *Nat. Biotechnol.*, 2001, **19**, 273.
15 S. F. Lim, R. Riehn, W. S. Ryu, N. Khanarian, C.-k. Tung, D. Tank and R. H. Austin, *Nano Lett.*, 2006, **6**, 169.
16 M. Nyk, R. Kumar, T. Y. Ohulchanskyy, E. J. Bergey and P. N. Prasad, *Nano Lett.*, 2008, **8**, 3834.
17 B. E. Cohen, *Nature*, 2010, **467**, 407.
18 F. Wang, *et al.*, *Nature*, 2010, **463**, 1061.
19 D. A. Parthenopoulos and P. M. Rentzepis, *Science*, 1989, **245**, 843.
20 E. Downing, L. Hesselink, J. Ralston and R. Macfarlane, *Science*, 1996, **273**, 1185.
21 F. Wang, R. Deng, J. Wang, Q. Wang, Y. Han, H. Zhu, X. Chen and X. Liu, *Nat. Mater.*, 2011, **10**, 968.
22 A. M. Ibarra-Ruiz, D. C. Rodríguez Burbano and J. A. Capobianco, *Advances in Physics: X*, 2016, **1**, 194.
23 S. Gai, C. Li, P. Yang and J. Lin, *Chem. Rev.*, 2014, **114**, 2343.
24 N. M. Idris, M. K. G. Jayakumar, A. Bansal and Y. Zhang, *Chem. Soc. Rev.*, 2015, **44**, 1449.
25 T. Saeed and P. O'Brien, *Thin Solid Films*, 1995, **271**, 35.
26 L. E. Greene, M. Law, J. Goldberger, F. Kim, J. C. Johnson, Y. Zhang, R. J. Saykally and P. Yang, *Angew. Chem., Int. Ed.*, 2003, **42**, 3031.
27 M. Kokotov, A. Biller and G. Hodes, *Chem. Mater.*, 2008, **20**, 4542.
28 R. R. Gadde and H. A. Laitinen, *Anal. Chem.*, 1974, **46**, 2022.
29 J. Zhang, L. Sun, H. Pan, C. Liao and C. Yan, *New J. Chem.*, 2002, **26**, 33.
30 J. Zhang, L. Sun, C. Liao and C. Yan, *Chem. Commun.*, 2002, 262.
31 J. Zhang, L. Sun, J. Yin, H. Su, C. Liao and C. Yan, *Chem. Mater.*, 2002, **14**, 4172.
32 J. Zhang, L.-D. Sun, X.-C. Jiang, C.-S. Liao and C.-H. Yan, *Cryst. Growth Des.*, 2004, **4**, 309.
33 D.-F. Zhang, L.-D. Sun, J.-L. Yin, C.-H. Yan and R.-M. Wang, *J. Phys. Chem. B*, 2005, **109**, 8786.
34 D.-F. Zhang, L.-D. Sun, J. Zhang, Z.-G. Yan and C.-H. Yan, *Cryst. Growth Des.*, 2008, **8**, 3609.
35 D. Yue, W. Lu, L. Jin, C. Li, W. Luo, M. Wang, Z. Wang and J. Hao, *Nanoscale*, 2014, **6**, 13795.
36 Z.-P. Zhang, *et al.*, *Nanoscale*, 2016, **8**, 15744.
37 S. B. Zhang, S.-H. Wei and A. Zunger, *J. Appl. Phys.*, 1998, **83**, 3192.
38 S. B. Zhang, S. H. Wei and A. Zunger, *Phys. Rev. B: Condens. Matter Mater. Phys.*, 2001, **63**, 075205.
39 J. Robertson and S. J. Clark, *Phys. Rev. B: Condens. Matter Mater. Phys.*, 2011, **83**, 075205.
40 S. J. Clark, J. Robertson, S. Lany and A. Zunger, *Phys. Rev. B: Condens. Matter Mater. Phys.*, 2010, **81**, 115311.
41 A. F. Kohan, G. Ceder, D. Morgan and C. G. Van de Walle, *Phys. Rev. B: Condens. Matter Mater. Phys.*, 2000, **61**, 15019.
42 A. Janotti and C. G. Van de Walle, *Phys. Rev. B: Condens. Matter Mater. Phys.*, 2007, **76**, 165202.

Open Access Article. Published on 19 April 2017. Downloaded on 9/18/2024 11:04:37 AM.
This article is licensed under a Creative Commons Attribution-NonCommercial 3.0 Unported Licence.

Open Access Article. Published on 19 April 2017. Downloaded on 9/18/2024 11:04:37 AM.
This article is licensed under a Creative Commons Attribution-NonCommercial 3.0 Unported Licence.

43 C. G. Van de Walle, *Phys. Rev. Lett.*, 2000, **85**, 1012.
44 A. Janotti and C. G. Van de Walle, *Nat. Mater.*, 2007, **6**, 44.
45 S. J. Clark and J. Robertson, *Phys. Rev. B: Condens. Matter Mater. Phys.*, 2010, **82**, 085208.
46 J. M. Khoshman and M. E. Kordesch, *Thin Solid Films*, 2007, **515**, 7393.
47 S. Lany and A. Zunger, *Phys. Rev. Lett.*, 2004, **93**, 156404.
48 S. Lany and A. Zunger, *Phys. Rev. B: Condens. Matter Mater. Phys.*, 2005, **72**, 035215.
49 B. Huang, *Phys. Chem. Chem. Phys.*, 2016, **18**, 13564.
50 B. Huang, *Phys. Chem. Chem. Phys.*, 2016, **18**, 25946.
51 B. Huang and M. Sun, *Phys. Chem. Chem. Phys.*, 2017, **19**, 9457.
52 D. V. Lang and R. A. Logan, *Phys. Rev. Lett.*, 1977, **39**, 635.
53 R. M. Rubinger, J. C. Bezerra, E. F. Chagas, J. C. González, W. N. Rodrigues, G. M. Ribeiro, M. V. B. Moreira and A. G. de Oliveira, *J. Appl. Phys.*, 1998, **84**, 3764.
54 E. R. Viana, J. C. González, G. M. Ribeiro and A. G. de Oliveira, *J. Phys. Chem. C*, 2013, **117**, 7844.
55 H. J. Queisser and D. E. Theodorou, *Phys. Rev. B: Condens. Matter Mater. Phys.*, 1986, **33**, 4027.
56 H. J. Queisser, *Phys. Rev. Lett.*, 1985, **54**, 234.
57 J. Clark Stewart, D. Segall Matthew, J. Pickard Chris, J. Hasnip Phil, I. J. Probert Matt, K. Refson and C. Payne Mike, *Z. Kristallogr.*, 2005, vol. 220, p. 567.
58 L. Kleinman and D. M. Bylander, *Phys. Rev. Lett.*, 1982, **48**, 1425.
59 S. G. Louie, S. Froyen and M. L. Cohen, *Phys. Rev. B: Condens. Matter Mater. Phys.*, 1982, **26**, 1738.
60 I. Grinberg, N. J. Ramer and A. M. Rappe, *Phys. Rev. B: Condens. Matter Mater. Phys.*, 2000, **62**, 2311.
61 A. M. Rappe, K. M. Rabe, E. Kaxiras and J. D. Joannopoulos, *Phys. Rev. B: Condens. Matter Mater. Phys.*, 1990, **41**, 1227.
62 N. Marzari, D. Vanderbilt and M. C. Payne, *Phys. Rev. Lett.*, 1997, **79**, 1337.
63 B. Huang, R. Gillen and J. Robertson, *J. Phys. Chem. C*, 2014, **118**, 24248.
64 M. I. J. Probert and M. C. Payne, *Phys. Rev. B: Condens. Matter Mater. Phys.*, 2003, **67**, 075204.
65 I. A. Vladimir, F. Aryasetiawan and A. I. Lichtenstein, *J. Phys.: Condens. Matter*, 1997, **9**, 767.
66 S. Lany and A. Zunger, *Phys. Rev. B: Condens. Matter Mater. Phys.*, 2009, **80**, 085202.
67 S. Lany and A. Zunger, *Phys. Rev. B: Condens. Matter Mater. Phys.*, 2010, **81**, 205209.
68 B. J. Morgan and G. W. Watson, *J. Phys. Chem. C*, 2010, **114**, 2321.
69 P. R. L. Keating, D. O. Scanlon, B. J. Morgan, N. M. Galea and G. W. Watson, *J. Phys. Chem. C*, 2011, **116**, 2443.
70 B. Huang, *Philos. Mag.*, 2014, **94**, 3052.
71 B. Huang, *J. Comput. Chem.*, 2016, **37**, 825.
72 B. Huang, *Phys. Chem. Chem. Phys.*, 2017, **19**, 8008.
73 S. Lany and A. Zunger, *Phys. Rev. B: Condens. Matter Mater. Phys.*, 2008, **78**, 235104.
74 D. B. Laks, C. G. Van de Walle, G. F. Neumark, P. E. Blöchl and S. T. Pantelides, *Phys. Rev. B: Condens. Matter Mater. Phys.*, 1992, **45**, 10965.
75 S.-H. Wei, *Comput. Mater. Sci.*, 2004, **30**, 337.
76 G. Makov and M. C. Payne, *Phys. Rev. B: Condens. Matter Mater. Phys.*, 1995, **51**, 4014.
77 B. Huang, *Solid State Commun.*, 2016, **237–238**, 34.
78 F. Oba, A. Togo, I. Tanaka, J. Paier and G. Kresse, *Phys. Rev. B: Condens. Matter Mater. Phys.*, 2008, **77**, 245202.
79 B. Huang, *Solid State Commun.*, 2016, **230**, 49.
80 F. Tuomisto, V. Ranki, K. Saarinen and D. C. Look, *Phys. Rev. Lett.*, 2003, **91**, 205502.
81 D. C. Look, J. W. Hemsky and J. R. Sizelove, *Phys. Rev. Lett.*, 1999, **82**, 2552.
82 J. Anderson and G. V. d. W. Chris, *Rep. Prog. Phys.*, 2009, **72**, 126501.
83 S. Lany and A. Zunger, *Phys. Rev. B: Condens. Matter Mater. Phys.*, 2010, **81**, 113201.
84 B. Huang, *Inorg. Chem.*, 2015, **54**, 11423.
85 B. Parthapratim, D. N. Tafen, F. Inam, C. Bin and D. A. Drabold, *J. Phys.: Condens. Matter*, 2009, **21**, 084207.
86 A. Roy, Y.-T. Cheng and M. L. Falk, *J. Phys. Chem. C*, 2016, **120**, 2529.
87 M. Dutta, S. Sarkar, T. Ghosh and D. Basak, *J. Phys. Chem. C*, 2012, **116**, 20127.
88 J. O. Hwang, D. H. Lee, J. Y. Kim, T. H. Han, B. H. Kim, M. Park, K. No and S. O. Kim, *J. Mater. Chem.*, 2011, **21**, 3432.
89 Y. Y. Hui, G. a. Tai, Z. Sun, Z. Xu, N. Wang, F. Yan and S. P. Lau, *Nanoscale*, 2012, **4**, 3118.
90 Q. Yao, Y. Liu, R. Lu, C. Xiao, K. Deng and E. Kan, *RSC Adv.*, 2014, **4**, 17478.
91 W. Hu, Z. Li and J. Yang, *J. Chem. Phys.*, 2013, **138**, 124706.
92 W. Geng, X. Zhao, H. Liu and X. Yao, *J. Phys. Chem. C*, 2013, **117**, 10536.
93 W. Geng, X. Zhao, W. Zan, H. Liu and X. Yao, *Phys. Chem. Chem. Phys.*, 2014, **16**, 3542.
94 S. Lany and A. Zunger, *Phys. Rev. B: Condens. Matter Mater. Phys.*, 2009, **80**, 085202.
95 S. Lany and A. Zunger, *Phys. Rev. B: Condens. Matter Mater. Phys.*, 2010, **81**, 205209.
96 F. Xiao, R. Chen, Y. Q. Shen, Z. L. Dong, H. H. Wang, Q. Y. Zhang and H. D. Sun, *J. Phys. Chem. C*, 2012, **116**, 13458.
97 J.-W. Lo, W.-C. Lien, C.-A. Lin and J.-H. He, *ACS Appl. Mater. Interfaces*, 2011, **3**, 1009.
98 S. Hirata and M. Head-Gordon, *Chem. Phys. Lett.*, 1999, **314**, 291.
99 P. Dorenbos, *J. Lumin.*, 2004, **108**, 301.
100 P. Dorenbos, *Chem. Mater.*, 2005, **17**, 6452.
101 P. Dorenbos, *Phys. Rev. B: Condens. Matter Mater. Phys.*, 2012, **85**, 165107.
102 P. Dorenbos and E. van der Kolk, *SPIE Proc.*, 2007, 647313.
103 G. H. Dieke, H. M. Crosswhite and H. Crosswhite, *Spectra and energy levels of rare earth ions in crystals*, Interscience Publishers, New York, 1968.
104 W. T. Carnall, G. L. Goodman, K. Rajnak and R. S. Rana, *J. Chem. Phys.*, 1989, **90**, 3443.
105 P. Tanner, in *Lanthanide Luminescence*, ed. P. Hänninen and H. Härmä, Springer Berlin Heidelberg, 2011, vol. 7, p. 183.

This journal is © the Owner Societies 2017

106 C. A. Morrison and R. P. Leavitt, *J. Chem. Phys.*, 1979, **71**, 2366.
107 D. Wang, G. Xing, M. Gao, L. Yang, J. Yang and T. Wu, *J. Phys. Chem. C*, 2011, **115**, 22729.
108 Q. Yu, T. Ai, L. Jiang, Y. Zhang, C. Li and X. Yuan, *RSC Adv.*, 2014, **4**, 53946.
109 H. Akazawa and H. Shinojima, *J. Appl. Phys.*, 2016, **120**, 123101.
110 Y. Yang, Y. Li, C. Wang, C. Zhu, C. Lv, X. Ma and D. Yang, *Adv. Opt. Mater.*, 2014, **2**, 240.
111 H. Ennen, J. Schneider, G. Pomrenke and A. Axmann, *Appl. Phys. Lett.*, 1983, **43**, 943.
112 Y. Pu, F. Xu, Z. Jiang, Z. Ma, F. Lu and D. Chen, *Appl. Phys. Lett.*, 2012, **101**, 191903.
113 Y.-F. Wang, L.-D. Sun, J.-W. Xiao, W. Feng, J.-C. Zhou, J. Shen and C.-H. Yan, *Chem. – Eur. J.*, 2012, **18**, 5558.
114 H. Dong, L.-D. Sun and C.-H. Yan, *Chem. Soc. Rev.*, 2015, **44**, 1608.
115 S. J. A. Pope, B. J. Coe, S. Faulkner, E. V. Bichenkova, X. Yu and K. T. Douglas, *J. Am. Chem. Soc.*, 2004, **126**, 9490.
116 Q. Chen, X. Xie, B. Huang, L. Liang, S. Han, Z. Yi, Y. Wang, Y. Li, D. Fan, L. Huang and X. Liu, *Angew. Chem., Int. Ed.*, 2017, DOI: 10.1002/anie.201703012R1.
117 Y. Liu, W. Luo, R. Li, G. Liu, M. R. Antonio and X. Chen, *J. Phys. Chem. C*, 2008, **112**, 686.
118 H. W. Leverenz, *Science*, 1949, **109**, 183.
119 H. W. Leverenz, *Science*, 1967, **157**, 414.
120 D. C. Rodriguez Burbano, E. M. Rodriguez, P. Dorenbos, M. Bettinelli and J. A. Capobianco, *J. Mater. Chem. C*, 2014, **2**, 228.
121 D. C. Rodríguez Burbano, S. K. Sharma, P. Dorenbos, B. Viana and J. A. Capobianco, *Adv. Opt. Mater.*, 2015, **3**, 551.

Open Access Article. Published on 19 April 2017. Downloaded on 9/18/2024 11:04:37 AM.
This article is licensed under a Creative Commons Attribution-NonCommercial 3.0 Unported Licence.